THESIS FOR THE DEGREE OF DOCTOR OF PHILOSOPHY
IN
THERMO AND FLUID DYNAMICS

Modal Analysis of Supersonic Flow Separation in Nozzles

by

RAGNAR LÁRUSSON

Department of Applied Mechanics
Division of Fluid Dynamics
CHALMERS UNIVERSITY OF TECHNOLOGY

Gothenburg, Sweden 2017

Modal Analysis of
Supersonic Flow Separation in Nozzles
RAGNAR LÁRUSSON
ISBN 978-91-7597-542-9

© Ragnar Lárusson, 2017

Doktorsavhandlingar vid Chalmers tekniska högskola
Ny serie nr. 4223
ISSN 0346-718X

Department of Applied Mechanics
Division of Fluid Dynamics
Chalmers University of Technology
SE-412 96 Gothenburg
Sweden
Telephone: +46 (0)31-772 1000

Cover:
Instantaneous velocity magnitude in a Detached Eddy Simulation of separated flow inside a truncated ideal contoured nozzle.

This document was typeset using LaTeX

Printed at Chalmers Reproservice
Gothenburg, Sweden 2017

Modal Analysis of Supersonic Flow Separation in Nozzles

RAGNAR LÁRUSSON

Department of Applied Mechanics
Division of Fluid Dynamics
Chalmers University of Technology

ABSTRACT

Operating a convergent-divergent nozzle under overexpanded conditions can lead to supersonic flow separation in the divergent section of the nozzle. In this case, an attached oblique shock wave forms at the separation base. The sudden pressure rise across the shock wave can cause damaging lateral pressure forces, or side-loads, to act on the nozzle if the separation line is asymmetric. Such asymmetry can be caused by downstream instabilities stemming from turbulence, external excitation or periodic modes.

The work reported in this thesis investigated the applicability of applying modal decomposition methods to supersonic nozzle flows. Axisymmetric RANS and URANS simulations of nozzle flows were investigated using the Arnoldi algorithm and Dynamic Mode Decomposition, respectively. The Arnoldi method relies on a linearized flow solver and has the advantage of being able to detect asymmetric modes on two dimensional grids. The DMD, however, is a snapshot based algorithm that needs no explicit linearization of the flow dynamics.

Results show that these methods can successfully be applied to supersonic nozzle flows with separation and strong shocks. For example, the Arnoldi method predicted a helical screeching mode with impressive accuracy and the DMD analysis of a perturbed two dimensional URANS flow field was able to detect modes linked to transonic resonance. Finally, Detached Eddy Simulations (DES) on a separated flow inside a Truncated Ideal Contoured Nozzle were performed for two separate nozzle pressure ratios (NPRs). The simulated side-loads were lower than experimentally measured values but within the uncertainty range. A three dimensional DMD analysis was made of the DES data and revealed a strong ovalization mode at the lower NPR and a helical mode which could be linked to a peak in side-load spectrum at the higher NPR.

Keywords: CFD, Separated Nozzle Flow, Dynamic Mode Decomposition, Arnoldi, Modal Analysis, Hybrid RANS-LES, Detached Eddy Simulation, RANS.

We must strive to be better than we are. It does not matter that we will never reach our ultimate goal. The effort yields its own rewards.

- Lt. Commander Data
From Star Trek: The Next Generation

Acknowledgements

No man is an island, John Donne famously wrote. Being a doctoral student is not only about doing research and writing papers. It is a great journey of personal development, unexpected challenges, defeats and victories, and it's all shaped by the people around you.

I begin by thanking those who gave me the chance to embark on this journey: my supervisors, Niklas Andersson, Lars-Erik Eriksson and Jan Östlund.

It's an honor to have been Niklas' first PhD student. I thank him for the trust he showed me and for always being available when I needed him. I have been further privileged as one of the last PhD students of Lars-Erik, who has recently retired from Chalmers. I thank him for his priceless guidance. And thank you Jan for always providing a new and positive view of my results.

I also want to thank Markus Olander Burak for his good help and discussions of the DMD method. And Arne Boman at GKN for always showing interest in my work and sending me interesting articles. Special thanks go to all my colleagues at GKN Aerospace in Trollhättan. I hated the commute but loved the company!

Thank you to Ralf Stark and Chloé Génin at DLR Lampoldshausen in Germany for welcoming me on my study visit there.

To all my colleages at Chalmers, past and present, I thank you for the good times we've had! Both at work and outside of it. The trips to Hemsedal and the trip to Munich were special treats. Ulla and Monica, thank you for all your help.

To my older Icelandic brothers at the division, Haukur, Eysteinn and Egill, I express my deep gratitude for everything we shared and for the things you taught me! I have tried to guide the newest member of our Icelandic CFD tribe, Elías. Everything he knows, I have taught him, just as everything I know you have taught me.

Special thanks go to my dear friend and colleague Amireza. He's just an awesome guy. Thank you as well to all of my friends in Sweden, those that remain and those that have moved on to other adventures.

I'm also blessed with many friends back home and I thank them for their friendship and being there for me whenever I come home for a visit. To my parents, who have made my life's journey possible, I am forever grateful for making me the person I am today. The love and encouragement all my family has shown me has been invaluable.

And to my wife Jóna, thank you for everything! You make me feel loved. The greatest feeling I know.

This research is funded by the Swedish National Space Board. Technical guidance from GKN Aerospace Sweden AB is also gratefully acknowledged.

Ragnar Lárusson
February 2017
Göteborg

List of publications

This thesis consists of an extended summary and the following appended papers:

Paper A R. Lárusson, N. Andersson, L.-E. Eriksson, and J. Östlund. Linear Stability Analysis Using the Arnoldi Eigenmode Extraction Technique Applied to Separated Nozzle Flow. *Proc. of the 49th AIAA/ASME/SAE/ASEE Joint Propulsion Conference* (2013). July 14-17, San Jose, CA, USA

Paper B R. Lárusson, N. Andersson, L.-E. Eriksson, and J. Östlund. Comparison of Eigenmode Extraction Techniques for Separated Nozzle Flows. *Proc. of the 50th AIAA/ASME/SAE/ASEE Joint Propulsion Conference* (2014). July 28-30, Cleveland, Ohio, USA

Paper C R. Lárusson, H. E. Hafsteinsson, N. Andersson, and L.-E. Eriksson. Investigation of Supersonic Jet Flow Using Modal Decomposition. *Proc. of the 20th AIAA/CEAS Aeroacoustics Conference* (2014). June 16-20, Atlanta, GA, USA

Paper D R. Lárusson, H. E. Hafsteinsson, N. Andersson, and L.-E. Eriksson. Investigation of Screech in Supersonic Jet Using Modal Decomposition. *Proc. of the 27th Nordic Seminar on Computational Mechanics* (2014). October 22-24, Stockholm, Sweden

Paper E R. Lárusson, N. Andersson, and J. Östlund. Dynamic Mode Decomposition of a Separated Nozzle Flow with Transonic Resonance. *AIAA Journal* (2017). Accepted for publication

Paper F R. Lárusson, N. Andersson, and J. Östlund. Hybrid RANS-LES Simulation of Separated Nozzle Flow. *Proc. of the 52nd AIAA/ASME/SAE/ASEE Joint Propulsion Conference* (2016). July 25-27, Salt Lake City, UT, USA

Paper G R. Lárusson, M. Olander Burak, N. Andersson, and J. Östlund. Dynamic Mode Decomposition Applied to a Detached-Eddy Simulation of Separated Nozzle Flow. *Proc. of AIAA SciTech Forum* (2017). January 9-13, Grapevine, TX, USA

Contents

Abstract **i**

Acknowledgements **v**

List of publications **vii**

Contents **ix**

I Extended Summary 1

1 Introduction **1**
1.1 Background 1
1.2 Motivation 2
1.3 Scope and Objective 3

2 Nozzle Flow **5**
2.1 Fundamentals and Fundamental History 5
2.2 Nozzle Flow Separation 9
2.3 Nozzle Side-Loads 12

3 Fluid Flow Equations **15**
3.1 The Navier-Stokes Equations and Equation of State 15
3.2 Computational Fluid Dynamics and Turbulence Modeling 16
3.3 Unsteady Favre-filtered Reynolds-averaged Navier-Stokes Equations (URANS) 17
3.3.1 The $k - \varepsilon$ Turbulence model 18
3.4 Detached Eddy Simulation (DES) 20
3.4.1 Background 20
3.4.2 Current Implementation 21
3.5 Discussion 22

4 Modal Decomposition **25**
4.1 The Arnoldi Algorithm and
the Dynamic Mode Decomposition 25

5 Numerical Methods and Tools **29**
5.1 Flow Solvers 29
5.1.1 Numerical Schemes 29
5.2 Arnoldi and DMD codes 29

6 Summary of Papers **31**
6.1 Paper A 31
6.2 Paper B 32

6.3 Paper C 32
6.4 Paper D 34
6.5 Paper E 34
6.6 Paper F 35
6.7 Paper G 36

7 Unpublished Results 37
7.1 Transient Nozzle Start-up Simulations 37
7.2 DMD Analysis of a TIC Nozzle. A Cooperation with DLR Lampoldshausen 45
7.2.1 Computational Set Up 45
7.2.2 Results 46
7.2.3 Discussion 47

8 Conclusions and Future Directions 53

References 55

II Appended Papers A–G 63

Part I
Extended Summary

1 Introduction

The chapter begins by emphasizing in Section 1.1 the importance and complexity of space travel and space industry and the role that the convergent-divergent nozzle plays in this context. Section 1.2 outlines the general motivation for the research and Section 1.3 presents the scope and objective of the thesis work.

1.1 Background

Escaping Earth's gravitational pull and venturing outside the safety of its atmosphere is one of the greatest and most extraordinary achievements of human kind. Only decades ago, in the early 1950s when the world's populations was just under 3 billion [8], global society functioned completely without space technology. Today, in 2017, with more than 7 billion people on the planet [8], we rely on it in an array of ways, most notably for navigation, weather forecast, traffic management and communication.

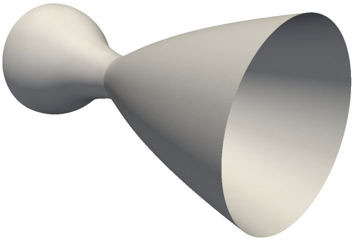

Figure 1.1: *Cylindrical Convergent-Divergent Nozzle.*

Space technology even affects our personal lives on a minute to minute basis as our smartphones and other gadgets frequently receive data from man-made satellites orbiting Earth. In 2015, the global space industry's economic activity amounted to approximately 323 billion US dollars [9], a number comparable to South Africa's annual gross domestic production in that year [10]. The industry's primary function is to build man-made satellites on Earth's surface and then deliver them to space to fulfill their purpose. Note that man-made satellites include the International Space Station, which hosts people, other animals and plants for an extended period of time.

The rockets that send these satellites to space are very sophisticated machines whose design, manufacturing and operation rely on almost all practiced engineering disciplines. The fundamental technology that propels rockets into space utilizes a momentum force acting between a fluid and a solid. To emphasize on the importance of this fluid-solid

interaction, it may be pointed out that we also rely on it to propel virtually all air and ground vehicles and to generate the major part of the world's electricity.
The way this momentum force is obtained varies between different technologies but, in the case of rocket propulsion, it is by using the convergent-divergent nozzle to accelerate pressurized gases to high velocities. This device, credited as the invention of Gustaf de Laval in the late 1800s [11], is traditionally cylindrical in shape with a cross-sectional area that varies in a way that allows for exhaust gases to accelerate. An example of such a nozzle is shown in Figure 1.1. This shows the VOLVO S6 research nozzle, which plays a central role in this thesis work. A real life example, the French Vulcain 2 rocket engine used on the European space launcher Ariane 5, is shown in Figure 1.2.

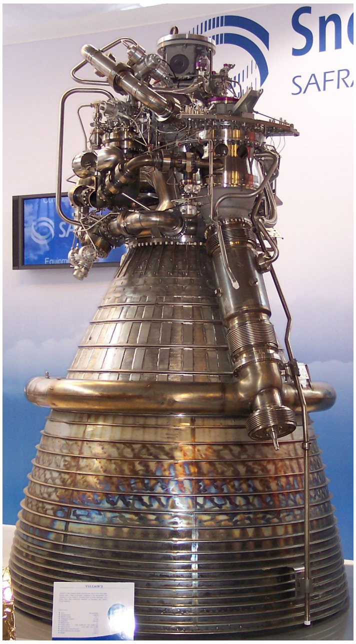

Figure 1.2: *The Vulcain 2 rocket engine.*

1.2 Motivation

Safety and robustness are two extremely important considerations in aeronautical and astronautical engineering. Propulsion efficiency, manufacturing and operating costs are other very important considerations that engineers must take into account. In all of this, weight plays a key roll and, allowing for some generalization and simplification, it can be stated that increased safety and robustness often demands increased weight, which in turn has an undesirable effect on efficiency and cost. To summarize, the design objective with regard to weight is to minimize it without compromising safety and robustness requirements. For space rockets, weight is exceptionally important because sending any mass into space demands tremendous energy and rocket designers seek to maximize the payload. There are other more technical and practical concerns for rocket engine design in particular, such as ease of handling and specifications for thrust vectoring systems [12]. For any machine to operate safely and consistently, it has to withstand thermal and mechanical loads, and engineers need to be able to predict these loads. Load prediction is based on understanding its source and the physical laws that dictate its behavior. Besides increasing operational safety, improved load prediction may also allow engineers to change their design to minimize or even completely eliminate certain loads. Minimizing loads, together with tighter, yet safe, design margins, makes possible lighter and more robust designs.

Almost every machine that we design interacts with a fluid, be it the ambient air, a surrounding body of water or internal gases and liquids. It is important to understand the interaction between a fluid and a mechanical component, especially when velocities, pressures or temperatures are high. Fluid flow instabilities can cause high loads, especially when they are periodic with frequencies that overlap with eigenfrequencies of structural components, which can result in load magnification. This is a source of great concern in space propulsion where flows are indeed high in speed, pressure and temperature. In particular, designers of rocket engines face the specific problem of nozzle side-loads. During start-up and shut-down of rocket engines, the propellant flow inside the nozzle separates from the nozzle walls and causes flow instabilities that result in lateral forces, or side-loads, to act on the nozzle structure. This phenomenon is the motivation behind the work in this thesis and will be described in more detail in Section 2.

There are several documented cases where side-loads have caused structural failure in rocket engine nozzles. The American Space Shuttle Main Engine (SSME) suffered failures of its propellant feeding lines during hot-firing testing in the later stages of its development [13]. Similarly, the Japanese LE-7 engine experienced failures of cooling tubes [14], and the gimbal block retaining bolts failed on the American J-2 engine during development [15]. The European Vulcain engine also experienced difficulties related to side-loads during its development [16]. Even though failures (or near-failures) occur during hot-fire testing while engines are still in the development phase, they can be extremely expensive to correct because of late design changes and additional testing. Nozzle side-loads can also influence the attitude dynamics of the rocket [17]. With this in mind, the benefits of accurately accounting for side-loads earlier in the design phase are obvious.

This is the greater context and motivation for this thesis work. The focus can be narrowed by defining the scope of the thesis.

1.3 Scope and Objective

This thesis work extends to three subfields of engineering research: nozzle flow studies, computational fluid dynamics (CFD) and modal decomposition methods. Here, the nozzle flow is the subject of the study while CFD and modal decomposition are the engineering tools used to simulate and analyze nozzle flows. The main objective was to investigate the applicability of modal decomposition methods in CFD to study separated nozzle flows. The primary nozzle flow studied was separated flow inside a truncated ideal contour (TIC) nozzle undergoing what is known as Free Shock Separation (FSS). Two dimensional (2D) axisymmetric Rreynolds-Averaged Navier-Stokes (RANS) and unsteady RANS (URANS) simulations of separated nozzle flows were analyzed using two types of modal decomposition methods. These were the Arnoldi algorithm and the Dynamic Mode Decomposition method, respectively. This is reported in appended Papers A and B. Three dimensional Detached-Eddy Simulations (DES) of the same nozzle were made and are reported in Paper F. The DMD algorithm was used to analyze the DES results in Paper G. In Papers C and D, a supersonic jet produced by a slightly overexpanded conical convergent-divergent nozzle was studied using DMD on data from a previously performed Large Eddy Simulation [18] and the results were compared with results from the Arnoldi algorithm applied to 2D-RANS simulations of the same nozzle. The DMD successfully extracted a mode associated with supersonic screech tone, while the Arnoldi predicted the same mode with impressive accuracy. Transonic resonance in a small expansion ratio conical nozzle was predicted and studied applying the DMD algorithm to 2D-URANS simulation data in paper E.

In total, three different nozzles flow types were studied in this work, using two types of CFD methods and two modal decomposition algorithms. The appended papers provide details on the methods used and the results. However, the following chapters aim to provide a short introduction to supersonic nozzle flow and the computational methods used in the thesis, respectively, as a supplement to the papers. A summary of the papers is also provided followed by previously unpublished results from a DES of a start-up transient and an additional 2D-URANS DMD analysis, respectively.

2 Nozzle Flow

This chapter begins by introducing the very fundamentals of supersonic nozzle flow and its early history in Section 2.1. Although nozzle design is not the topic of the thesis, it is helpful to become familiar with the parameters and flow characteristics that are important for nozzle performance. Following the introduction to nozzle flow, Section 2.2 covers the basics of nozzle flow separation. The focus here will be on free shock separation (FSS), which is the only type of separation covered in this thesis. A discussion of side-loads in particular is provided in Section 2.3

2.1 Fundamentals and Fundamental History

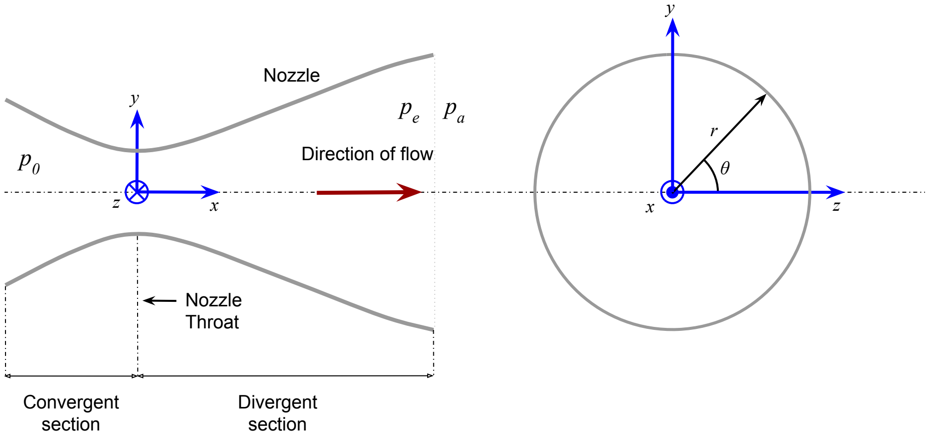

Figure 2.1: *Definition of an axisymmetric convergent-divergent nozzle.*

As Anderson demonstrates in his book *Modern Compressible Flow with Historical Perspective* [11], the following equation can be derived from quasi one-dimensional flow equations:

$$\frac{dA}{A} = (M^2 - 1)\frac{du}{u} \tag{2.1}$$

The equation states that, for a compressible isentropic flow through a duct, an increase in cross sectional area A results in a decrease in velocity u if the Mach number, M, is lower than unity. This is very familiar to us in everyday life; who hasn't squeezed the end of a garden hose to increase the velocity of the water jet coming out of it? What is not so familiar to most of us is the other truth this equation reveals: that an *increase* in area A causes an *increase* in velocity if the Mach number is greater than one!

Gustav de Laval experienced this first hand in 1888 when he significantly improved the performance of his impulse steam turbine by adding a divergent section to the convergent nozzle that propelled the turbine blades, creating the first convergent-divergent nozzle. However, he was not familiar with the equation above and, in fact, initially, it was disputed whether the flow was indeed supersonic within the divergent section. The existence of supersonic flow inside the divergent section was not confirmed until Aurel Stodola published the first scientific experiments on convergent-divergent nozzles in 1903, confirming the shock theory of Rankine and Hugoniot from a few decades earlier [11]. Figure 2.1 shows a schematic definition of an axisymmetric convergent-divergent nozzle that operates as follows: highly pressurized gas with total pressure p_0 enters the convergent section at low subsonic velocities and is accelerated by decreasing the cross-sectional area until it reaches sonic conditions ($M = 1$) at the throat from which, in accordance with Equation 2.1, it is further accelerated to supersonic velocities by expanding the area in the divergent section. It is the difference between the inlet total pressure, p_0, and the external ambient pressure, p_a, that drives the flow through the nozzle. The ambient pressure is often also referred to as the back pressure, and the ratio p_0/p_a is the nozzle pressure ratio (NPR). Figure 2.2 shows the development of the flow properties along the axis of a supersonic nozzle. The throat is located at $x = 0.0$, and all flow variables have been normalized with their respective throat values. In the figure we see how the pressure, density and temperature drop as the flow accelerates and expands.

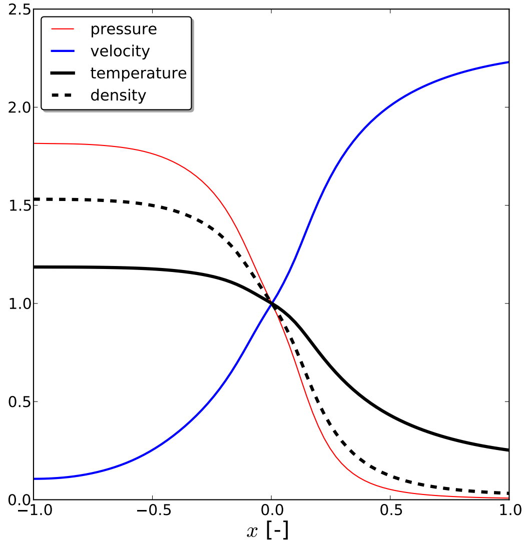

Figure 2.2: *Flow properties along the axis of a convergent-divergent nozzle. The throat is located at* $x = 0.0$ *and all flow variables have been normalized with their respective throat values.*

Although de Laval's and Stodola's work with nozzles was intended to improve the performance of impulse steam turbines, the primary application that motivates the current work is rocketry. A rocket is a flight vehicle that propels itself by using the reacting forces created by expelling part of its mass at high speeds. The mass expelled is the rocket propellant, composed of a fuel and an oxidizer that are burned within a combustion chamber to create the hot[1] and highly pressurized exhaust gas which is expelled from the nozzle exit at high speeds to achieve maximum thrust. The thrust obeys Newton's second law, which states that the rate of change of momentum of an object is equal to the force acting on it:

$$F = \frac{dm}{dt} v_e \tag{2.2}$$

This method of propulsion has been known to man since at least the 13th century when the first solid propellant rockets were used by the Chinese as a part of their ”fire” arrows [20]. In 1813, the English mathematician William Moore published equations describing the motion of rockets, including the famous delta-v equation. Moore's efforts were intended for military applications, but the first man to envision the use of rockets for space exploration was the Russian schoolteacher and visionary Konstantin Tsiolkovsky, who also independently derived the delta-v equation and published it in 1903. The delta-v equation describes how the change in a space vehicle velocity, ΔV, in the absence of gravity or any other body forces, is connected to its initial mass, m_0, including the propellant, its final mass, m_f, after the propellant has been expelled, and the effective propellant exhaust velocity, v_e:

$$\Delta V = v_e \ln \frac{m_0}{m_f} \tag{2.3}$$

It is important to hold the initial mass, m_0, of a rocket to a minimum to reduce the energy needed to reach orbit. The force equation (Eq. 2.2) and the delta-v equation (Eq. 2.3) both tell us that m_0 can be lowered, while keeping F or ΔV constant, by increasing the exhaust velocity, v_e. It was the American rocket pioneer Robert H. Goddard who first realized that the de Laval nozzle could be used to achieve high rocket exhaust velocities, and he proceeded to build the world's first liquid rocket engine in 1926 [21].

The thrust, F, created by a nozzle is given as:

$$F = \dot{m} v_e + (p_e - p_a) A_e \tag{2.4}$$

where $\dot{m}$ is the mass flow rate through the nozzle and v_e is the exhaust velocity, p_e is the static pressure at the nozzle exit, p_a is the ambient pressure and A_e is the nozzle's exit cross sectional area.

Note that Equation 2.4 is Equation 2.2 plus an added term accounting for the pressure mismatch between the ambient air and the exhaust. For an ideally expanded flow, the pressure at the nozzle exit, p_e, is equal to the ambient pressure, p_a, making the second term in Equation 2.4 zero. If the ambient pressure is lower than the exit pressure, $p_a < p_e$, the flow is said to be *underexpanded* and, in the case where the ambient pressure is higher than the exit pressure, $p_a > p_e$, the flow is said to be *overexpanded*. Both cases are undesirable because the highest potential exhaust velocity is not achieved in an underexpanded flow and, in an overexpanded flow, the second term in Equation 2.4 is negative, decreasing the thrust. Under highly overexpanded conditions, there is a risk of flow separation.

---

[1] High combustion temperature and pressure together with low molecular weight of the exhaust gas improves the nozzles performance [19].

Two fundamental parameters that are frequently used in rocket engine design and theory are the specific impulse, I_{sp}, and the expansion ratio[2], ε.

The specific impulse is defined as:

$$I_{sp} = \frac{F}{\dot{m}}$$

It is a simple measure of rocket engine performance that compares the engine thrust to its mass flow rate. For an idelly expanded nozzle flow $I_{sp} = v_e$ and in that case we can replace v_e with I_{sp} in Equation 2.3 and truly appreciate its importance to rocket efficiency. In the form above, its unit is m/s but it is commonly normalized with Earth's gravitational constant $g = 9.81m/s^2$, giving it a unit of seconds [22]. A typical first stage engine has a specific impulse between $300s$ and $450s$.

The expansion area is defined as the ratio between the exit cross-sectional area and throat cross-sectional area:

$$\varepsilon = \frac{A_e}{A_t}$$

A high expansion ratio is desired as it maximizes exhaust velocities. However, at sea level, the ambient air pressure limits this due to a potential flow separation, as will be covered in the next section. A practical limitation exists as well, as a high expansion ratio means a high exit diameter with associated packaging challenges.

The first rocket engine nozzles were typically conical in shape as this made for easier design and manufacturing [23]. These nozzles, however, were not very efficient compared to modern nozzle contours. An "ideal" nozzle contour can be created with the aid of method of characteristics (MOC). These contours provide a isentropic and shock-free supersonic gas expansion with a uniform exit velocity profile. However, these nozzles are extremely long and consequently heavy and difficult to install [22]. Shortening such a nozzle proves to be a good way to reduce weight without suffering significant thrust losses; these nozzles are called truncated ideal contoured nozzles, or TIC nozzles. The VOLVO S6 nozzle which is the subject of Papers A, B, F and G, is a TIC nozzle, while the nozzles in Papers C, D and E are conical nozzles. Conical nozzles are not used today on high-thrust liquid propellant rocket engines, but some modern jet engines have conical exhaust nozzles. However, they were used in the current thesis only as a legacy from previous research efforts on which Papers C, D and, E are based, *i.e.* Zaman *et al.* [24] and Hafsteinsson *et al.* [25]. TIC nozzles have been used on rocket engines in the past but are not commonplace. However, they are a common subject of research and are a potential choice for future rocket engines given their low side-load levels compared to other common contours [26].

On the basis of a previously developed theory by Guderley and Hantsch [27][3], Rao [28] published a paper on how to derive a nozzle contour for optimal thrust by using the method of characteristics. These nozzles, usually referred to as thrust optimized contoured nozzles (TOC), significantly increased geometrical efficiency compared to a 15° half angle conical nozzle with the same expansion ratio[4]. Rao later proposed a skewed parabolic approximation to TOC nozzles [29][3], referred to as thrust optimized parabolic (TOP) nozzles. The TOC nozzle produces weak compression waves along the wall which coalesce into an internal shock wave further away from the wall. In comparison, TOP nozzles produce an internal shock at the wall due to a discontinuity formed at the intersection between a circular arc at the throat and the parabolic curve that defines the rest of the divergent section. Interestingly, this leads to increased wall pressure in TOP nozzles compared to TOC nozzles, giving TOP nozzles a higher resistance to flow separation [22]. TOP nozzles are commonly used on rocket engines and were *e.g.* employed on the American Space Shuttle Main Engine and the European Vulcain engine [22].

---

[2] Not to be confused with turbulent dissipation, ε, a turbulence model variable presented in next chapter.

[3] As reported in Östlund and Muhammad-Klingmann [22].

Östlund and Mohammad-Klingmann [22] give more details on these nozzle types in addition to others, such as compressed truncated ideal contoured nozzles (CTIC) and directly optimized nozzles, which are obtained using more advanced computational methods that consider viscous effects.

The axisymmetric cylindrical nozzle is virtually the only nozzle type that has been used on space vehicles and, although other nozzle shapes exist, they remain concept ideas. Interested readers are referred to Östlund and Muhammad-Klingmann [22] for more detail on novel nozzle concepts. Hagmemann *et al.* [30] also published an interesting paper on advanced nozzle concepts, such as a plug nozzle with external ambient expansion.

2.2 Nozzle Flow Separation

Under highly overexpanded conditions, when the nozzle wall pressure goes down to approximately 80% to 40% of the ambient pressure[5], the boundary layer can not sustain the adverse pressure gradient and the flow separates from the nozzle wall, causing a standing shock wave to form at the separation base. Depending on the nozzle contour and pressure ratio, the separation can be classified as either a restricted shock separation (RSS) in which the separated flow reattaches to the wall, forming a closed circulation bubble downstream of the shock, or a free shock separation (FSS) where the separated flow does not reattach to the wall, creating a separation zone that extends all the way to the exit of the nozzle, allowing the ambient air to enter the separated region [22].

Nave and Coffey [31] discovered the existence of RSS during the development of the American J-2S engine in the early 1970s. They discovered the flow separation pattern transitions from FSS to RSS during an engine start-up and found that this transition causes a high increase in side-load levels. Now it is understood that restricted shock separation appears in TOC/TOP nozzles due to the presence of the internal shock [32]. Typically, during a start-up of a TOC/TOP nozzle, FSS is experienced at low NPRs and later transitions into RSS at higher NPRs. Ideal contours feature no internal shocks and RSS is therefore absent in such nozzles. Details of RSS are skipped here because the

---

[4] A 15° half angle conical nozzle is commonly used to compare nozzle performance.

[5] This can vary depending on the nozzle Mach number at the incipient separation location but values are anywhere from 25% to 80% [22].

current work does not feature a TOP or a TOC nozzle but can be found *e.g.* in refs. [22, 32, 33].
Figure 2.3 schematically shows the main features of a free shock separation. An oblique shock wave forms at the separation base creating a Mach reflection at the centerline forming the Mach disc, a shock wave normal to the incoming flow and a reflected shock called the ”triple shock” where the oblique shock and the Mach disc meet.

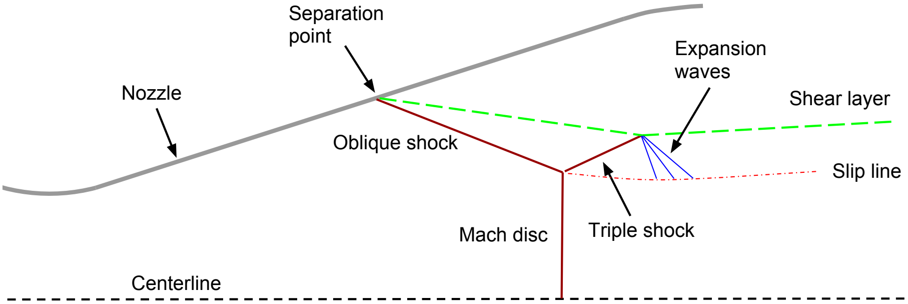

Figure 2.3: *Shock pattern of supersonic flow with free shock separation inside an axisymmetric convergent-divergent nozzle.*

The triple shock extends into a supersonic shear layer which envelopes the jet’s core. The jet flow undergoes a series of expansion and compression waves until the jet becomes sub-sonic, as can be seen in the average Mach number field shown in Figure 2.4.

Figure 2.5 shows a schematic of the free shock separation close to the wall. The adverse pressure gradient between the ambient and the wall pressure is communicated through the subsonic parts of the attached boundary layer. At the incipient separation point, x_i, the boundary layer begins to thicken and a series of weak compression waves form and coalesce into a separation shock [22, 26]. The nozzle flow is directed towards the centerline by the shock, indicated by red lines in Figure 2.5, while ambient air enters the separated region and flows towards the separation point until it is redirected into the shear layer, as indicated with the blue lines in the figure.

The wall pressure change across the separation is schematically shown in Figure 2.6. As the flow expands, the pressure follows a typical decrease until it undergoes a sudden rise across the separation zone between x_i and x_p, where it reaches a plateau value p_p from which it slowly increases to about 85% to 95% of the ambient pressure, p_a, at the nozzle exit, x_e. Point x_i marks the incipient of the separation and x_s marks the actual separation point. The distance between x_i and x_s is the separation length, while the shock wave boundary layer interaction (SWBLI) length is between x_i and x_p.

Supersonic flow separation always involves SWBLI, a highly dynamic, essentially three dimensional flow phenomenon. SWBLI is relevant for a range of applications, particularly within aerospace, and basic research on the topic remains active. Similarities can be

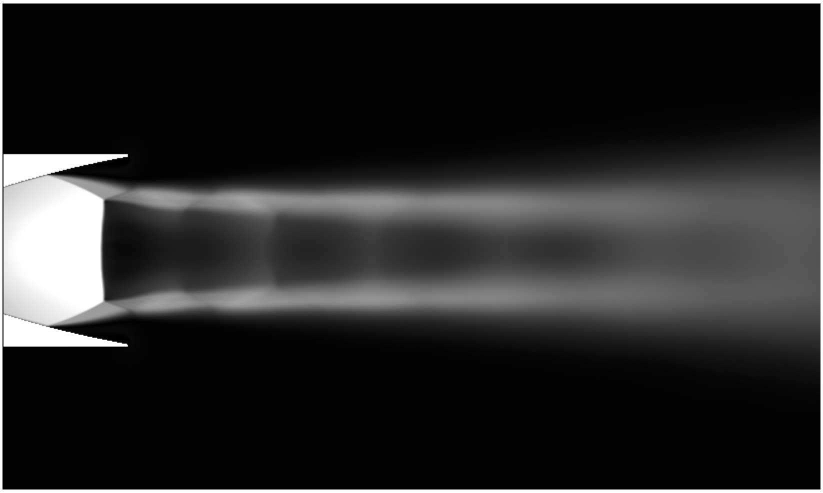

Figure 2.4: *Average Mach number field featuring free shock separation. From a Detached Eddy Simulation (DES) of the VOLVO S6 nozzle reported in appended Paper F.*

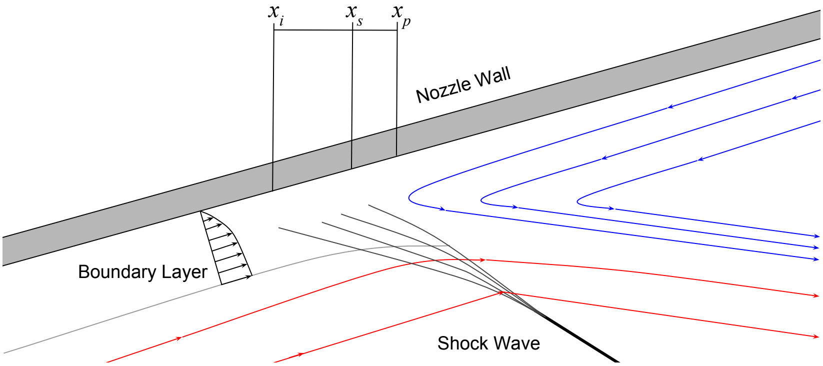

Figure 2.5: *Free shock separation at nozzle wall.*

drawn between the FSS featured in nozzles and shock induced separations in cases such as forward-facing step [34], compression ramp [35] and impinging shock [36]. The pressure rise across the separation is indeed similar in all cases [37][6], along with the pressure's spectral density across the interaction length [22]. SWBLI studies have furthermore shown that the shock motion frequency is also one to two orders of magnitude lower compared to the characteristic frequency of the incoming boundary layer [38] and the significance of the incoming boundary layer instability on the shock motion is not completely understood.

---

[6] As cited in [26].

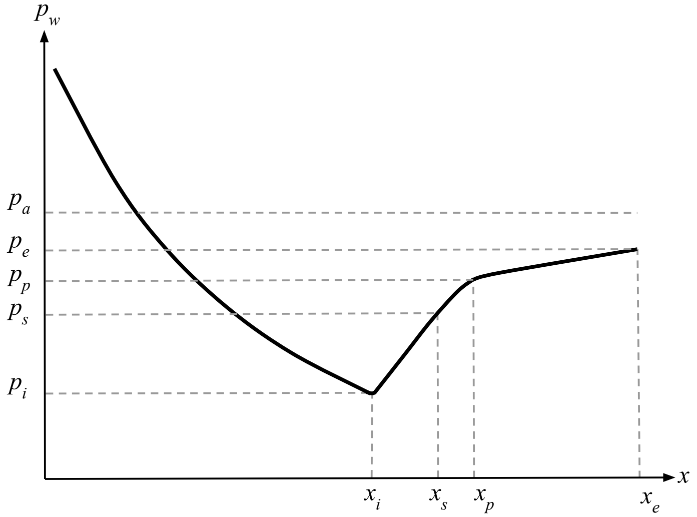

Figure 2.6: *Schematic representation of nozzle wall pressure during free shock separation. The figure is intended to show trends and is not to scale.*

2.3 Nozzle Side-Loads

As covered in the first chapter, the main motivation for this work is the lateral forces, or side-loads, that can cause harmful strain on the nozzle structure and other engine components. They are in principle caused by asymmetrical flow separation where the high pressure rise across the shock and the imbalance in its distribution along the circumference give rise to side-loads. As early as the 1940s, engine developers faced problems with nozzle flow separation [23], but the issue has enjoyed increased attention in the past few decades. Nave and Coffey [31] observed in their experiment a high increase in side-loads during the FSS-RSS transition that the nozzle experienced during an increase in NPR. Mattsson *et al.* [39] later discovered that an RSS-FSS transition can occur as the separation approaches the nozzle exit. An increase in side-loads as the separation front moves through the nozzle exit is frequently observed and is termed the end-effect. As mentioned in the preceding section, FSS-RSS transition is limited to TOC/TOP nozzles and is not present in TIC nozzles; consequently, these do not suffer such high side-load levels. However, experiments have proven that side-loads in TIC nozzles are not negligible [40, 41], and Stark and Wagner [40] and Stark and Génin [42] have identified flow processes that lead to a side-load increase in a TIC nozzle such as transition of the boundary layer near the throat and a consequent partial reattachment. In addition to this, unstable inflow, turbulence in the downstream jet, external pressure buffeting and aeroelastic coupling are all factors that can lead to an increase in side-loads.

Significant effort has been made in the past to create semi-empirical side-load models [22]. However, as these models provide insight into the causes of side-loads, they provide moderate accuracy, and prediction methods based in first principles such as using computational fluid dynamics are desired since these methods can simulate turbulence and other flow processes responsible for the side-loads. Modern computers and simulation methods continue to develop and provide a good opportunity to perform numerical simulations of supersonic nozzle flows in order to better understand the flow phenomenon itself and to further develop efficient simulation techniques. Of course, this work is already well under way, and there are several examples of high fidelity simulations on separated nozzle flows [43–50], but further work is always needed. In this thesis, the attention has been on modal decomposition methods that could reveal undamped modes of frequencies close to structural eigenfrequencies of engine components or the nozzle itself. It can furthermore shed light on the mechanics of periodic flow instabilities that could give rise to damaging forces. The importance of experimental results for validation of computational methods cannot be understated. Many efforts in the past have provided invaluable data for validation [40, 41, 51–54] and continued efforts are needed to provide further insight into side-load mechanics.

Nozzle side-loads set limitations to the expansion ratio of a modern nozzle. Their design needs to assure high enough wall pressure to avoid separation due to high ambient pressure. However, as a rocket ascends, the ambient conditions change quickly with lower atmospheric pressure and there is much to be gained in terms efficiency if the nozzle flow could adapt to the changing environment [22]. For example, Aghababaie and Theunissen [26] point out that a TIC nozzle with high expansion ratio could possibly function in a separated mode, adjusting to change in ambient pressure as the rocket ascends. To help such interesting ideas come to fruition, better side-load prediction methods would be of tremendous help.

3 Fluid Flow Equations

This chapter covers the flow equations on which the simulations in this thesis are based. We begin in Section 3.1 by presenting the Navier-Stokes equations and thermodynamic relationships from which the RANS and DES equations are derived. Section 3.2 introduces the concept of turbulence modeling and the motivation behind it. The URANS equations and the k–ε model are presented in Section 3.3 and the Detached Eddy Simulation implementation used in this work is presented in Section 3.4. Additional discussion is provided in Section 3.5.

3.1 The Navier-Stokes Equations and Equation of State

The Navier-Stokes equations consist of the continuity, the momentum and the energy equations. In Einstein notation they can be written as

$$\frac{\partial \rho}{\partial t} + \frac{(\partial \rho u_j)}{\partial x_j} = 0 \tag{3.1}$$

$$\frac{\partial(\rho u_i)}{\partial t} + \frac{\partial(\rho u_i u_j)}{\partial x_j} = -\frac{p}{\partial x_i} + \frac{\partial \sigma_{ij}}{\partial x_j} \tag{3.2}$$

$$\frac{\partial(\rho e_0)}{\partial t} + \frac{\partial(\rho e_0 u_j)}{\partial x_j} = -\frac{\partial(p u_j)}{\partial x_i} + \frac{\partial}{\partial x_j}\left(C_p \frac{\mu}{Pr}\frac{\partial T}{\partial x_j}\right) + \frac{\partial(u_j \sigma_{ij})}{\partial x_j} \tag{3.3}$$

where ρ, u, p, e_0 are density, velocity, pressure, and total internal energy, respectively. The total internal energy is defined as

$$e_0 = e + \frac{u_k u_k}{2}$$

The viscous stress, σ_{ij}, is given by

$$\sigma_{ij} = \mu\left(2S_{ij} - \frac{2}{3}S_{mm}\delta_{ij}\right) \tag{3.4}$$

where the strain-rate tensor, S_{ij}, is

$$S_{ij} = \frac{1}{2}\left(\frac{\partial u_i}{\partial x_j} + \frac{\partial u_j}{\partial x_i}\right) \tag{3.5}$$

and the Prandtl number, Pr, is defined as

$$Pr = \frac{\mu C_p}{\lambda} \tag{3.6}$$

where C_p is the specific heat at constant pressure[7] and μ is the dynamic viscosity, both assumed in this thesis to be constant. As the Prandtl number is specified for the simulations, the thermal conductivity, λ, does not need to be specified explicitly. All the simulations in the thesis simulate air flow at temperatures ranging from 285 K to 400 K and, within this range, it can be assumed that the gas is calorically perfect [11], meaning that the the ideal gas law can be applied[8]:

---

[7] Similarly C_v is the specific heat at constant volume.

$$p = \rho R T$$

where R is the gas constant.
The following relationship between temperature, T, internal energy, e, enthalpy, h, and the specific heats applies:

$$\begin{aligned} e &= C_v T \quad (3.7) \\ h &= C_p T \quad (3.8) \\ C_v &= C_p - R \quad (3.9) \end{aligned}$$

3.2 Computational Fluid Dynamics and Turbulence Modeling

The Navier-Stokes equations describe the full range of scale present in fluid flows, including the finest scales of turbulence [55]. However, with the exception of cases where the equations can be greatly simplified, there exists no known analytical solution to the equations. Computational Fluid Dynamics (CFD) is therefore an important research field and an engineering tool that deals with solving the Navier-Stokes equations numerically. Direct Numerical Simulations, commonly known as DNS, attempt to solve the flow equations presented in the preceding section and, in order to achieve accurate solutions, the DNS need to resolve the motion of the finest turbulent eddies. This requires the computational grid used to obtain the numerical solution to be fine enough to capture the geometrical features of the smallest turbulent eddies, and the time step the solver takes needs to be small enough to capture their dynamics. For high speed, wall-bounded flows of engineering interest, the range of scales is so wide that the computational cost of resolving the whole turbulence spectra is too high to be economically feasible or even possible to perform. This has led to the field of turbulence modeling, where the objective is to either model the effect of the *whole* turbulence spectrum on the mean flow or to model the effects of the *parts* of the spectrum that contain the finer scales of turbulence on the resolved spectrum.

---

[8] The ideal gas law can also be used for thermally perfect gases with varying gas constant R.

3.3 Unsteady Favre-filtered Reynolds-averaged Navier-Stokes Equations (URANS)

Modeling the effects of turbulence on the mean flow is usually done by decomposing the flow variables according to Reynolds decomposition,

$$\phi = \overline{\phi} + \phi'$$

where the flow variable ϕ is decomposed into its mean component $\overline{\phi}$ and its fluctuating component ϕ'. This decomposition, or separation of scales, can be applied to the Navier-Stokes equations to derive the Reynolds-averaged Navier-Stokes equations (RANS). When dealing with compressible flows, it is convenient to use Favre-filtering to avoid having to model extra terms in the Reynolds-averaged continuity equation [56]. A Favre-filtered flow quantity $\tilde{\phi}$ is density weighted such that

$$\tilde{\phi} = \frac{\overline{\rho\phi}}{\overline{\rho}}$$

and the following decomposition applies:

$$\phi = \tilde{\phi} + \phi''$$

where ϕ'' can be thought of as the high frequency component and $\tilde{\phi}$ as the low frequency component of the flow variable ϕ.
Using this, the Unsteady[9] Favre-filtered Reynolds-averaged Navier-Stokes (URANS) equations can be formulated:

$$\frac{\partial\overline{\rho}}{\partial t} + \frac{\partial(\overline{\rho}\tilde{u}_j)}{\partial x_j} = 0 \tag{3.10}$$

$$\frac{\partial(\overline{\rho}\tilde{u}_i)}{\partial t} + \frac{\partial(\overline{\rho}\tilde{u}_i\tilde{u}_j)}{\partial x_j} = -\frac{\partial\overline{p}}{\partial x_i} + \frac{\partial\overline{\sigma}_{ij}}{\partial x_j} + \frac{\partial\tau_{ij}}{\partial x_j} \tag{3.11}$$

$$\begin{aligned} \frac{\partial\left(\overline{\rho}\tilde{e}_0\right)}{\partial t} + \frac{\partial\left(\overline{\rho}\tilde{e}_0\tilde{u}_j\right)}{\partial x_j} = &- \frac{\partial(\overline{p}\tilde{u}_j}{\partial x_j)} + \frac{\partial}{\partial x_j}\left(C_p\frac{\mu}{Pr}\frac{\partial\tilde{T}}{\partial x_j} + q_j^t\right) + \frac{\partial}{\partial x_j}\left(\overline{u_i\sigma_{ij}}\right) \\ &- \frac{1}{2}\frac{\partial}{\partial x_j}\overline{\rho}\left(\widetilde{u_iu_iu_j} - \widetilde{u_iu_i}\tilde{u}_j\right) \end{aligned} \tag{3.12}$$

The Favre-filtered viscous stress tensor reads

$$\overline{\sigma}_{ij} = \mu\left(2\tilde{S}_{ij} - \frac{2}{3}\tilde{S}_{mm}\delta_{ij}\right) \tag{3.13}$$

---

[9] Note that we allow for time variation in the equations and therefore $\overline{\phi}$ is not a long-term mean component of ϕ. This is important for the URANS-DMD analysis and the DES implimentation.

and the Favre-filtered strain rate tensor is

$$\tilde{S}_{ij} = \frac{1}{2}\left(\frac{\partial \tilde{u}_i}{\partial x_j} + \frac{\partial \tilde{u}_j}{\partial x_i}\right) \tag{3.14}$$

Two additional terms have now appeared, the turbulent stress tensor, τ_{ij}, and the turbulent heat flux term, q_j^t.

The turbulent stress tensor is

$$\begin{aligned} \tau_{ij} =& -\overline{\rho}\left(\widetilde{u_i u_j} - \tilde{u}_i \tilde{u}_j\right) \\ =& -\overline{\rho}\left(\underbrace{\left(\widetilde{\tilde{u}_i \tilde{u}_j} - \tilde{u}_i \tilde{u}_j\right)}_{I} + \underbrace{\left(\widetilde{u_i'' \tilde{u}_j} + \widetilde{\tilde{u}_i u_j''}\right)}_{II} + \underbrace{\widetilde{u_i'' u_j''}}_{III}\right) \end{aligned} \tag{3.15}$$

Terms *I-III* are called the Leonard stresses, cross stresses and Reynolds stresses, respectively. Similar to τ_{ij}, the turbulent heat flux is given as

$$\begin{aligned} q_j^t =& -C_p\overline{\rho}\left(\widetilde{T u_j} - \tilde{T}\tilde{u}_j\right) \\ =& -C_p\overline{\rho}\left(\widetilde{\tilde{T}\tilde{u}_j} - \tilde{T}\tilde{u}_j + \widetilde{T''\tilde{u}_j} + \widetilde{\tilde{T}u_j''} + \widetilde{T''u_j''}\right) \end{aligned} \tag{3.16}$$

Two terms remain to be addressed in the energy equation, *i.e.* the product $\overline{u_i \sigma_{ij}}$ can be replaced with $\tilde{u}_i(\overline{\sigma}_{ij} + \tau_{ij})$ and the last term in the energy equation is considered negligible and is dropped. The Navier-Stokes equations form a closed set of equations but in the derivations of the URANS equations two new terms in the momentum and the energy equations appear that need to be modeled. Those are the turbulent stress terms, which include the unresolved high frequency components of velocity and temperature, respectively, and are therefore related to unresolved turbulence.
These terms need to be modeled, and the following section presents the $k-\varepsilon$ turbulent model formulation that was used in this thesis.

3.3.1 The $k-\varepsilon$ Turbulence model

The $k-\varepsilon$ model by Launder and Spalding [57] is an eddy viscosity model and, like other eddy viscosity models, it is based on the Boussinesq assumption that proposes a linear relationship between the turbulent stresses and the mean flow gradients through an eddy viscosity, μ_t, also known as the turbulent viscosity. Based on this assumption, the turbulent stress tensor can be modeled as

$$\tau_{ij} = \mu_t\left(2\tilde{S}_{ij} - \frac{2}{3}\frac{\partial \tilde{u}_k}{\partial x_k}\delta_{ij}\right) - \frac{2}{3}\overline{\rho}\tilde{k}\delta_{ij} \tag{3.17}$$

and the turbulent heat flux tensor is model is based on a simple diffusion term:

$$q_j^t = C_p \frac{\mu_t}{Pr_t} \frac{\partial \tilde{T}}{\partial x_j} \tag{3.18}$$

where P_t is the turbulent Prandtl number. The $k - \varepsilon$ turbulence model gives the turbulent viscosity as

$$\mu_t = C_\mu \overline{\rho} \frac{\tilde{k}^2}{\tilde{\varepsilon}}, \tag{3.19}$$

The modeled turbulent kinetic energy, $\tilde{k}$, and dissipation $\tilde{\varepsilon}$, are obtained by solving their respective modeled transport equations:

$$\frac{\partial \overline{\rho} \tilde{k}}{\partial t} + \frac{\partial}{\partial x_j} \left(\overline{\rho} \tilde{k} \tilde{u}_j - \left(\mu + \frac{\mu_t}{\sigma_k} \right) \frac{\partial \tilde{k}}{\partial x_j} \right) = P_k - \overline{\rho} \tilde{\varepsilon} \tag{3.20}$$

and,

$$\frac{\partial \overline{\rho} \tilde{\varepsilon}}{\partial t} + \frac{\partial}{\partial x_j} \left(\overline{\rho} \tilde{\varepsilon} \tilde{u}_j - \left(\mu + \frac{\mu_t}{\sigma_\varepsilon} \right) \frac{\partial \tilde{\varepsilon}}{\partial x_j} \right) = \left(C_{\varepsilon 1} P_k - C_{\varepsilon 2} \overline{\rho} \tilde{\varepsilon} \right) \frac{\tilde{\varepsilon}}{\tilde{k}} \tag{3.21}$$

P_k is the turbulence production term and C_μ, σ_k, σ_ε, $C_{\varepsilon 1}$ and $C_{\varepsilon 2}$ are model constants. Regarding boundary conditions, some relatively low values are usually prescribed for k and ε at inflow boundaries. At walls, $k = 0$ and $\partial \varepsilon / \partial y = 0$ where y is the direction normal to the wall.
The production of turbulence is modeled according to

$$P_k = \left(\mu_t \left(2\tilde{S}_{ij} - \frac{2}{3} \frac{\partial \tilde{u}_k}{\partial x_k} \delta_{ij} \right) - \frac{2}{3} \overline{\rho} \tilde{k} \delta_{ij} \right) \frac{\partial \tilde{u}_i}{\partial x_j} \tag{3.22}$$

and, in the current work, a realizable constraint is applied to the turbulent viscosity:

$$\mu_t = \min \left(C_\mu \overline{\rho} \frac{\tilde{k}^2}{\tilde{\varepsilon}}, \frac{C_r \overline{\rho} \tilde{k}}{\sqrt{\tilde{S}_{ij} \tilde{S}_{ij}}} \right) \tag{3.23}$$

where C_r is a constant.

A standard log-law wall function was used in all simulations for two reasons. Firstly, the linearized solver proved to be unstable when a low-Reynolds number turbulence model was used, most likely because of high gradients near the wall. Secondly, the separation point was accurately predicted using the wall function so its use was continued in the DES and URANS simulations to save computational time. A low-Re turbulence model requires a fine enough grid resolution in the wall normal direction to be able resolve the flow gradients in the boundary layer all the way to the wall, requiring the first grid point to be at $y^+ < 1$. Wall functions serve as a compromise between accuracy and computational cost and only require the first grid point outside of the wall to be located in the logarithmic layer [58]; the first grid point can be between $y^+ > 30$ and $y^+ < 100$. When the log-law wall function is used, it is assumed that the velocity profile follows the log-law, as in a fully developed boundary layer[10]:

$$\frac{\tilde{u}_t}{u_\tau} = \frac{1}{\kappa} \ln(y^+) + B \tag{3.24}$$

where κ is the Von Kárman constant, B is a constant. $u_\tau = \sqrt{(\tau_w/\overline{\rho})}$ is the friction velocity, τ_w is the wall shear stress and

$$y^+ = \frac{\overline{\rho} y u_\tau}{\mu}$$

is the normalized wall distance. The log-law wall function is activated if $y^+ \gtrsim 10.7$ and, when activated, the wall shear stress, τ_w, is adjusted to fulfill Equation 3.24, see Davidson [58] for more detail.

When the turbulence model is activated, pressure $\overline{p}$ and temperature $\tilde{T}$ are computed according to:

$$\overline{p} = (\gamma - 1)\overline{\rho} \left(\tilde{e}_0 - \frac{\tilde{u}_k \tilde{u}_k}{2} - \tilde{k} \right) \tag{3.25}$$

and

$$\tilde{T} = \frac{1}{C_v} \left(\tilde{e}_0 - \frac{\tilde{u}_k \tilde{u}_k}{2} - \tilde{k} \right) \tag{3.26}$$

where $\gamma = C_p/C_v$.

3.4 Detached Eddy Simulation (DES)

3.4.1 Background

The $k - \varepsilon$ model used in the URANS simulations was designed to model the effects of the whole turbulence spectrum on the mean flow and, subsequently, only low frequency transients can be captured, regardless of how fine the computational grid is. Conversely, Large Eddy Simulations (LES) are designed to model only the finest scales of turbulence while resolving the larger energy containing scales by separating the scales using a filter. The filter is usually based on the grid density and the unresolved scales are consequently called sub-grid scales (sgs). The same filtered formulation of the continuity, momentum and energy equations applies for both LES and URANS simulations. The difference between the methods lies in how the turbulent stresses are modeled and, more specifically, when both the URANS and LES use a turbulence model based on the Boussinesq assumption, the difference lies solely in how the turbulent viscosity, μ_t, is obtained. The most common model used in LES is the algebraic Smagorinsky model [59] or the Favre-filtered compressible version of it by Erlebacher *et al.* [60]. Other more elaborate models involve solving a transport equation for turbulent quantities such as the k-equation model by Yoshizawa [61]. The simple algebraic model by Smagorinsky tends to work well on fine enough grids as the sgs scales are assumed to be isotropic and are simpler to model. In fact, an LES approach called implicit LES uses only numerical diffusion[11] for the sgs modeling [62].

---

[10] An assumption which is often false and should be made with caution.

The turbulent viscosity in LES is considerably lower than in URANS simulations, resulting in lower modeled turbulent stresses. Because the total turbulent stress levels (modeled plus resolved) remain constant, low modeled stresses trigger formation of resolved stresses to keep this balance. To acquire an accurate solution in an LES, the grid resolution must be fine enough for the filter to cut off small enough scales that are appropriate for the sgs model. As the wall is approached, the turbulent structures become smaller and, in the process, the grid resolution requirement for an accurate LES become stricter. For this reason, Spalart proposed Detached Eddy Simulation as a hybrid between RANS and LES, a simulation method that operates in URANS mode in attached boundary layers and in LES mode further away from walls and in separated regions [63]. This method simply involves a length scale substitution in the turbulence model. The turbulent length scale as defined by the RANS model, L_{RANS}, is replaced with a DES length scale, L_{DES}, which switches between an LES length scale, L_{LES}, and the RANS length scale depending on which is smaller. Spalart applied this to the one-equation Spalart-Allmaras model which solves a transport equation for the turbulent field variable $\tilde{\nu}$ [64]. There, the DES length scale is inserted into the destruction term of the $\tilde{\nu}$-equation, replacing the turbulent length scale of that model, which is simply the distance from the nearest wall boundary. DES has enjoyed much success as a hybrid RANS-LES method; it is widely used and has been extended to other eddy-viscosity models, most notably to the two-equation Menter-SST model [65]. In this thesis, the DES length scale substitution has been applied to the $k-\varepsilon$ model presented in the previous section.

3.4.2 Current Implementation

In this work, the DES length scale is inserted into the destruction term of the k transport equations and into the expression for the turbulent viscosity, μ_t, as shown by Yan *et al.* [66], and is recommended for nozzle flow by Shams *et al.* [67].

The RANS and the LES length scales, respectively, are

$$L_{RANS} = C_\mu^{3/4}\frac{\tilde{k}^{3/2}}{\tilde{\varepsilon}} \tag{3.27}$$

and

$$L_{LES} = C_{DES}\Delta \tag{3.28}$$

where $C_{DES} = 0.5$ and Δ is the average grid cell dimension

$$\Delta = average(\Delta_x, \Delta_y, \Delta_z)$$

---

[11] An added diffusion caused by truncation errors in the numerical scheme. The level of this diffusion varies depending on the scheme but it is present in all CFD simulations.

Here, the DES length scale follows the Delayed DES (DDES) variant by Spalart *et al.* [68]:

$$L_{DES} = L_{RANS} - f_s \max(0, L_{RANS} - L_{LES}) \tag{3.29}$$

where f_s is a shielding function which prevents the equations from operating in LES mode within attached boundary layers. The choice of shielding function varies in the literature; for example, Menter and Kunts [69] used the F1 and F2 functions of the Menter-SST model and Spalart *et al.* [68] formed a shielding function applicable to any turbulent viscosity model.

The use of the universal shielding function by Spalart *et al.* [68] yielded a premature separation in the nozzle simulations. A novel vorticity based shielding function was developed instead:

$$f_s = 1 - \tanh(\mu|\omega|)(1 - \tanh((d_w/d_l)^2) \tag{3.30}$$

where $|\omega|$ is the vorticity magnitude, d_w is the distance from the nearest wall boundary and d_l is a wall distance limit beyond which f_s is 1.0. The performance of the shielding function is reported in Paper F.

After the length scale substitution, the k equation is as follows:

$$\frac{\partial \overline{\rho}\tilde{k}}{\partial t} + \frac{\partial}{\partial x_j}\left(\overline{\rho}\tilde{k}\tilde{u}_j - \left(\mu + \frac{\mu_t}{\sigma_k}\right)\frac{\partial \tilde{k}}{\partial x_j}\right) = P_k - \frac{C_\mu^{3/4}\overline{\rho}\tilde{k}^{3/2}}{L_{DES}} \tag{3.31}$$

And, similarly, the substitution in the μ_t equation results in:

$$\mu_t = \min\left(L_{DES}\, C_\mu^{1/4}\, \overline{\rho}\, \sqrt{\tilde{k}}\ ,\ \frac{C_r \overline{\rho}\tilde{k}}{\sqrt{\tilde{S}_{ij}\tilde{S}_{ij}}}\right) \tag{3.32}$$

3.5 Discussion

The choice of the value of the DES coefficient $C_{DES} = 0.5$ is discussed in Paper F. It is a lower value than the traditionally recommended values of approximately 0.65 [63, 66] and the reason for such a low value was to minimize the ”grey area” problem [68]. The grey area refers to the boundaries between the RANS and the LES regions and the problem with high turbulent viscosity levels being convected into the LES region, delaying the formation of resolved turbulence. To speed up the formation of turbulence, a relatively low value of C_{DES} was chosen for now, although this value needs to be calibrated using a test case such as decay of isotropic turbulence (DIT)[66]. The use of the vorticity based shielding function would also benefit from more scrutiny and could be tested on other test cases such as a compression ramp [35] or a 2-D periodic hill [70] to see how well it shields the attached boundary layer in these cases and whether the separation front reacts to downstream disturbances.

No universal turbulence model exists and every model has its benefits and limitations. The use of the $k - \varepsilon$ served its purpose adequately within the scope of this thesis work, but anyone wanting to explore the potential of numerically simulating nozzle flows should keep in mind the wide selection of turbulence models that exists. Not uncommon in nozzle flow simulations are Menter's k–ω Shear Stress Transport model [65] and the one-equation Spalart-Allmaras model [64]. There are many papers, review articles and textbooks that cover the topic of turbulence modeling and Davidson [55] gives an excellent overview of both fluid dynamics and turbulence modeling in his extensive lecture notes, which are available to anyone with access to the internet. Furthermore, Bredberg provides a compact and accessible overview of two-equation eddy viscosity models [71].

4 Modal Decomposition

Perturbations with sufficiently low amplitudes behave in a linear fashion and a linearization of the flow dynamics can therefore be used to describe the evolution of small perturbations introduced to the system. Small periodic perturbations are relevant because a flow field's response to them can be magnified through resonance.

Analytical models of resonance in nozzle flow have been made in the past and most notable is perhaps the work by Wong [72], in which a perturbative quasi-one-dimensional inviscid theory coupled with a dual oscillator concept was used to model the shock movement and resonance.While the results do agree well with experimental and numerical data, the model was not put forth as a replacement for experiments and numerical simulations. Rather, its role was meant to compliment them as a quick estimation tool and to add insight into the rudimentary mechanisms behind the phenomena. Despite the usefulness of analytical models such as in [26, 72, 73], they involve major simplifications regarding the geometry and the flow physics and more sophisticated models are thus desired.

In the work presented in this thesis, the applicability of two different eigenvalue algorithms coupled with an axisymmetric RANS solver to predict the eigenmodes of separated supersonic flow inside a axisymmetric convergent-divergent nozzle has been investigated. These are the Arnoldi and the Dynamic Mode Decomposition (DMD) algorithms.

These methods are indeed superior to analytical methods in terms of modeling the flow physics and considering the nozzle geometry. They do, however, require more effort in terms of preprocessing, computation and post processing, but, compared to full three dimensional resolved simulations, they are still very affordable[12].

A detailed description of these algorithms and the nozzle flow cases is provided in the appended papers. Section 4.1 provides a short discussion and comparison of the Arnoldi and DMD algorithms.

4.1 The Arnoldi Algorithm and the Dynamic Mode Decomposition

The Arnoldi algorithm was originally developed by Walter Edwin Arnoldi and published in 1951 as a method to approximate eigenvalues of large matrices [74]. It belongs to a family of algorithms referred to as *Krylov methods* [75]. The idea is to avoid explicit use of the large matrix being studied by vector mapping and subsequent orthogonal projection of the mapped vectors onto a Krylov subspace. This produces a projection matrix of reduced size, which can be subjected to direct eigendecomposision. Using a subspace of sufficient size, some of the eigenvalues of the reduced matrix will converge to good approximations of the eigenvalues of the significantly larger system matrix.

In the present study the large matrix governs the temporal development of the linearized flow system. This large matrix is not known as such, but the vector mapping can be achieved by running a linearized flow solver. This precise method has been used successfully in a range of applications involving compressible flow, see [76–79]. The Arnoldi algorithm has been applied as well to incompressible flow, see for example [80] and [81]. In fact, the algorithm, being a well known technique in the field of applied mechanics, has a wide span of applications, for example in nano science [82], material science [83] and chemistry [84].

---

[12] Here, the DMD of 2D-URANS data is referred to. DMD can of course be applied to 3D simulations as is done in Paper G.

The Dynamic Mode Decomposition (DMD) is an Arnoldi-like method which does not require linearization of the flow dynamics but relies on a set of observation data from a flow simulation or experimental measurements. In the algorithm, a Singular Value Decomposition (SVD) of the data is performed and a projection of the full flow system onto the left singular vector base[13] can be computed without using the large underlying, unknown system matrix.

Since the DMD was first presented at a conference in 2008 [85] and shortly after published by Schmid [86] and Rowley *et al.* [87] it has been well received and used in a variety of flow analyses, see for example [79, 88–91]. Significant effort has been made as well towards strengthening its theoretical foundation, see [92–94], and new variants have been introduced [92, 95–98]. A comprehensive discussion of the theory and applications of the DMD can be found in [94].

In the work presented in this thesis, the DMD has been applied to flow field snapshots from both 2D-URANS and DES simulations of the nozzle flow. What separates the URANS-DMD analysis in the current study from much other published work on applied DMD analysis, such as [86, 89–91, 94], is that a disturbance is introduced to a relatively steady flow field and the response and stabilization is sampled in contrast to sampling a naturally unstable flow, as is done in the DMD of the DES data in Paper G.

Both the DMD and the Arnoldi algorithms compute a projection of the full flow dynamics onto a orthogonal vector basis, which describes the dynamics of its linear approximation. However, as described above, they do this in very different ways. The key differences are listed below; while some aspects of these points are true in general, this list is meant to be specific to the method and application described in this thesis:

- The linear solver used in the Arnoldi method does not include a turbulence model as the model equations are highly nonlinear and not suitable for linearization. A frozen eddy viscosity field has been used in some cases as a way to include effects from the mean flow turbulence [99]. However, attempts to apply a frozen eddy viscosity field resulted in divergence of the linear solver for the VOLVO S6 nozzle. This is possibly linked to a ripple found in the eddy viscosity field near foot of the separation shock.

- In contrast to the Arnoldi, the DMD requires no direct linearization of the flow dynamics and thus no mapping via a linear flow solver is needed. Instead, the DMD can be applied to sampled data from a nonlinear simulation. As a consequence, effects from the turbulence model and nonlinearity can be captured in the results. This is the focus of Paper B, where the two methods are compared. Furthermore, the results in Paper E show that the DMD captures harmonic modes that can only stem from nonlinear effects in the URANS solver. This would not be possible using the Arnoldi method.

---

[13] Also known as the Proper Orthogonal Decomposition (POD) base.

- Being an integrated part of the solver, the Arnoldi method has to be applied to all degrees of freedom, *i.e.* the whole geometry and computational domain and all flow variables, while using DMD we can focus on areas of interest and dismiss the rest of the domain. One can also choose which variables to feed into the algorithm. These can be solver variables or other derived variables.
- As the size of the Krylov projection basis is increased in the Arnoldi procedure, the number of reliable eigenmode approximations is increased. In contrast, as the number of snapshots is increased in the DMD, the number of reliable eigenmode approximations do not necessarily increase. This is because snapshots that are linearly dependent do not add any more information. Furthermore, the Arnoldi algorithm is known to display faster convergence as compared to the DMD [86].
- An advantage of the Arnoldi method is that, for a two dimensional, axisymmetric geometry and mean flow, the linearized equations can be formulated with azimuthal wavenumber. Using that formulation, it could detect possible asymmetric modes, which are of great interest from an engineering point of view. This is not possible with DMD applied to a two dimensional simulation. DMD can of course be applied to three dimensional data and detect asymmetric modes as in Paper G.

5 Numerical Methods and Tools

This chapter gives a brief overview of the numerical methods and tools used in this thesis.

5.1 Flow Solvers

In this thesis, all flow simulations were performed using a density based explicit compressible Navier-Stokes equaion solver. For all nonlinear flow simulations, that is the RANS/URANS simulations and the Detached Eddy Simulations, the G3D::Flow code was used (previously named volsol++ in Papers A, B, and C). G3D::Flow is a massively parallel code framework for CFD simulations, written in C++ and based on the parallel solvers and data types in the PETSc [100, 101] libraries, see [102] for more information regarding G3D::Flow. The linear flow simulations needed in the Arnoldi algorithm were performed using the Fortran in-house solver g2daxlnav, see [103]. This linear solver is a part of the G3D family of CFD codes, a precursor to G3D::Flow, see [104].

5.1.1 Numerical Schemes

In all flow simulations the flow equations have been solved numerically using a standard cell-centered control-volume scheme on a non-orthogonal block-structured grid using rectangular grid cells [104]. For the convective fluxes, a third-order upwind-biased scheme was used in the RANS/URANS simulations and a low-dissipation third-order upwind-biased scheme was used in the Detached Eddy Simulations. In all simulations, a second-order centered difference approach was used for diffusive fluxes. The time integration was carried out using a second-order accurate three-stage Runge-Kutta scheme. For shock handling, a pressure gradient controlled dissipation of Jameson type was used. These schemes are described in detail in [104].

5.2 Arnoldi and DMD codes

The Arnoldi analysis was performed using a Fortran code written by Lars-Erik Eriksson that incorporates his linear solver mentioned above. The standard numerical library Linear Algebra PACKage (LAPACK) was used for the eigendecomposition of the reduced system-matrix.

The DMD performed in Papers B to E was performed using the Python scripting language and the SciPy package of libraries for scientific computing in Python [105]. The DMD analysis in Paper G was performed using a massively parallel in-house developed code written in C++ which utilizes solvers and distributed data types available in the PETSc [100, 101] and SLEPc [106, 107] libraries.

6 Summary of Papers

The chapter gives summaries of the appended paper, outlining their aim and major results. Some additional comments are provided along with the division of work between authors.

6.1 Paper A

Linear Stability Analysis Using the Arnoldi Eigenmode Extraction Technique Applied to Separated Nozzle Flow

Aim: To investigate the applicability of the Arnoldi method to supersonic separated flow inside a nozzle.

Results: The method provided converged eigenmode with discrete frequencies. The frequency range of the least damped modes was within the frequency range in which experiments and numerical simulations have shown the flow to be most sensitive. Asymmetric modes were detected as well when running the linearized solver with an azimuthal wavenumber $m = 1$. The lower frequency modes showed movement of the shock pattern and, as the frequency increased, modes showed an increase in shear layer activity and an acoustic wave radiating from the separated region became visible. High frequency modes that showed fluctuations upstream of the separation were detected as well, but are linked to the nozzle geometry and gas properties rather than the flow separation.
The discrete frequency modes prove that there exists a closed feedback loop between the separation and the downstream jet. However, the shape and convergence properties of the eigenvalue spectrum also indicated a strong presence of continuous spectra in the flow stemming from pure downstream transport of instabilities.

Comments: The use of a frozen eddy viscosity field in the linear solver caused the solution to diverge and therefore could not be applied. As of now, the cause of this is unknown but inspection of the eddy viscosity field revealed a ripple in the field, slightly upstream of the separation point, which could be linked to the problem. The use of a linearized Euler solver (no viscosity at all) also proved unstable and, as a working solution, a linearized Navier-Stokes solver using only laminar viscosity was used.

Division of Work:
Ragnar Lárusson generated the computational mesh, set up and ran all simulations, post processed results and wrote the paper. Together the co-authors supervised and provided support regarding solvers and many other technical issues. They provided invaluable help with the analysis of the results and writing of the paper.

6.2 Paper B

Comparison of Arnoldi Eigenmode Extraction to Dynamic Mode Decomposition for a Separated Nozzle Flow

Aim: The DMD algorithm was applied to snapshots from an axisymmetric URANS simulation of the same nozzle flow investigated in Paper A, and the results were compared to the corresponding Arnoldi modes. The aim was to investigate the influence of excluding turbulence in the linearized solver on the Arnoldi results.

Results: In certain cases, DMD and Arnoldi produced almost identical modes with respect to frequency, damping and shape. This is very interesting given the difference between the methods in how they model the flow physics and build their projection basis. One possible reason could be that the bulk of the flow is not wall bounded and is therefore not greatly influenced by viscous effects.
Most of the DMD modes differed greatly from the Arnoldi modes, however. This is linked to nonlinear effects, modeled turbulence and the fact that the DMD is prone to producing modes that are spurious and contaminated by noise.
It should be noted that no similar modes to the to the Arnoldi modes with higher damping were found among the DMD modes. The reason for this might be that these modes are so damped in the URANS solver that they quickly drown out in the data or that the disturbance of the URANS flow did not excite those modes.

Comments: Experimenting with excluding singular vectors with the lowest singular values in the projection basis of the DMD proved to be useful for finding well resolved and reliable modes. This was done by changing the size of the projection basis to see which modes were relatively unaffected by the change. The unaffected modes are typically well resolved and reliable.

Division of Work: Ragnar Lárusson generated the computational mesh, set up and ran all simulations, wrote the DMD script and post processed results along with writing the paper. Together the co-authors supervised and provided support regarding solvers and many other technical issues. They provided invaluable help with the analysis of the results and writing of the paper.

6.3 Paper C

Investigation of Supersonic Jet Flow Using Modal Decomposition

Aim: Large Eddy Simulations of a slightly overexpanded supersonic jet had previously been performed at Chalmers in collaboration with the University of Cincinnati and GKN Aerospace in Sweden, see *e.g.* [25, 108–111]. This gave a perfect opportunity to apply the DMD algorithm to LES data and to compare with results from 2D-URANS DMD and Arnoldi analysis of the same case. The nozzle flow in this case had a relatively low nozzle pressure ratio of 4.0 and an exit Mach number of 1.58 and was not separated. In contrast to sampling a naturally unstable turbulent flow for the DMD algorithm, the LES flow field was excited with an axisymmetric fluidic injection at the nozzle exit and the response of the jet to the excitation was sampled. This was done to mimic the URANS DMD analysis which relies on an initial flow perturbation to capture the dynamics of the URANS.

Results: The Arnoldi analysis was performed with azimuthal wavenumber $m = 0$, which gives axisymmetric modes, and $m = 1$, which gives helical modes. The least damped Arnoldi mode overall was a helical mode with a frequency and acoustical radiation similar to the screech tone that this nozzle is known to produce. This screech mode was not captured with the LES-DMD because the fluidic injection failed to trigger it but, in a later study, presented in Paper D, this mode was detected using LES-DMD, see summary of Paper D below.
The least damped modes of the axisymmetric Arnoldi analysis and the URANS-DMD were virtually identical. This is an interesting result when keeping in mind that the Arnoldi method lacks all influence from nonlinear effects or the turbulence model (except in the reference solution). The more damped modes found in the Arnoldi analysis were absent in the URANS-DMD results. It is possible that, due to their high damping, they are drowned out in the URANS data and are therefore not detectable by the DMD.
The LES-DMD produced modes very similar to the 2D methods in terms of frequency and acoustic radiation. The LES modes were more damped than the modes from the 2D methods.

Comments: The LES data were sampled on a two dimensional plane along the symmetry axis since full three dimensional DMD was not feasible with the DMD code used. The fluidic injection used to excite the flow field was axisymmetric and, as a result, triggered only axisymmetric modes; therefore, the helical screech mode that this nozzle is known to produce was not triggered. Furthermore, the Arnoldi and the URANS-DMD analysis produced several modes that originated internally in the nozzle. These modes were not excited in the LES because the fluidic injection was applied at the nozzle exit. Due to problems with noise in the LES-DMD modes, the fluidic injection perturbation cycle was performed several times and the snapshots represented an average of the perturbation cycles. This seemed to have improved the resolution and, interestingly, the damping of low frequency modes decreased with more averaging. Given these effects, it is questionable whether such flow perturbation is needed or even advisable in this case; it would perhaps have been better to simply sample the naturally unstable LES flow field. Note that perturbing the URANS flow field was necessary in this case as the URANS simulation converged to a steady state.

Division of Work: Ragnar Lárusson generated the computational mesh, set up and ran the URANS-DMD and Arnoldi simulations, wrote the DMD script and post processed results along with writing the paper. Haukur E. Hafsteinsson, the second author, set up, ran and sampled the LES simulations. Together, all the co-authors supervised and provided support regarding solvers and many other technical issues. They provided invaluable help with the analysis of the results and writing of the paper.

6.4 Paper D

Investigation of Screech in Supersonic Jet Using Modal Decomposition

Aim: This short article, which was presented at the 27th Nordic Seminar on Computational Mechanics, can be viewed as a continuation of the work in Paper C. It features the same nozzle geometry but a slightly lower nozzle pressure ratio of 3.5, which is known to produce a particularly strong screeching tone at around 2.2 kHz. In contrast to the methodology applied in Paper C, the Large Eddy Simulation was sampled in this case without any added flow perturbation. The aim here was to see whether the DMD could extract the screeching mode from the LES snapshots and compare it with the screech mode found with the Arnoldi method.

Results: The screech mode extracted from the LES with the DMD algorithm was strikingly similar to the screeching mode obtained with the Arnoldi algorithm. Their frequency difference was around 4% and their acoustic radiation was nearly identical. The screech mode had a helical structure (azimuthal wavenumber $m = 1$) and would therefore not be detected using the URANS-DMD methodology. This demonstrates the advantage of the Arnoldi method, which can detect modes with higher azimuthal wavenumbers on two dimensional grids.

Comments: As in Paper C, the LES-DMD was not performed on full three dimensional data but on four two dimensional planes simultaneously, one longitudinal and three axial planes. This allowed the helical structure of the mode to be confirmed.

Division of Work: Ragnar Lárusson generated the computational mesh, set up and ran the Arnoldi simulations, wrote the DMD script and post processed results along with writing the paper. Haukur E. Hafsteinsson, the second author, set up, ran and sampled the LES simulations. Together all the co-authors supervised and provided support regarding solvers and many other technical issues. They provided invaluable help with the analysis of the results and writing of the paper.

6.5 Paper E

Investigation of a Separated Nozzle Flow with Transonic Resonance Using Dynamic Mode Decomposition

Aim: The aim of the study was to investigate whether the DMD algorithm, when applied data from an axisymmetric URANS simulations of a low area ratio conical nozzle, is capable of predicting the transonic resonance frequencies previously identified in studies reported by Zaman *et al.* [24] and Loh and Zaman [112].

Results: The DMD algorithm provided undamped, harmonic modes with frequencies close to those observed in the experiment by Zaman *et al.* [24]. The DMD modes showed a standing pressure wave inside the divergent part similar to what was suggested in [24]. It was concluded that the method applied in this study can predict the resonance frequencies with reasonable accuracy and, consequently, it can shed some light on the mechanism behind the phenomena. The results furthermore reveal that the primary mechanism responsible for the resonance is embedded in the two dimensional axisymmetric RANS equations.

Comments: The URANS simulation of the nozzle flow did not experience transonic resonance and converged to a stable solution. In order to capture the flow dynamics with the DMD algorithm, it was necessary to disturb the flow field.
The capability of the DMD to take into account nonlinear effects was demonstrated by the detection of harmonic modes.

Division of Work: Ragnar Lárusson generated the computational mesh, set up and ran all simulations, wrote the DMD script and post processed results along with writing the paper. Together, the co-authors supervised and provided support regarding solvers and many other technical issues. They provided invaluable help with the analysis of the results and writing of the paper.

6.6 Paper F

Hybrid RANS-LES Simulation of Separated Nozzle Flow

Aim: To investigate whether a Delayed Detached Eddy Simulation (DDES) using a realizable $k - \varepsilon$ turbulence model with a log-law wall function is capable of predicting side-loads on a TIC nozzle. The TIC nozzle used was the same as the one used in Papers A and B, namely the VOLVO S6 nozzle. Two nozzle pressure ratios were simulated: NPR=14.67 and NPR=19.74.

Results: The predicted side-loads are lower than measured values from a previous test campaign [113] although, they are within the uncertainty levels. This is expected since the DES models parts of the turbulent spectrum that could possibly contribute to the side-loads. However, it is possible that the use of the standard log-law wall function is the main reason for the lower side-load levels. Recommended future work would be to investigate other possible wall functions or repeat the simulations using a low Reynolds number turbulence model.

Comments: The use of a vorticity based boundary layer shielding function, which prevents the DES to operate in a LES mode in boundary layers, was successful in preventing premature separation. However, the wall pressure downstream of the separation was higher than predicted by URANS simulations, which were in excellent agreement with measured values.

Division of Work: Ragnar Lárusson generated the computational mesh, set up and ran all simulations, post processed results along with writing the paper. Together, the co-authors supervised and provided support regarding solvers and many other technical issues. They provided invaluable help with the analysis of the results and writing of the paper.

6.7 Paper G

Dynamic Mode Decomposition Applied to a Detached-Eddy Simulation of Separated Nozzle Flow

Aim: To investigate the capability of the DMD algorithm to extract important modes from data sampled from the DES presented in Paper F. A parallelized DMD code was used to perform the analysis and a full 3D analysis was therefore possible. Important modes were identified by using the sparsity-promoting algorithm by Jovanović *et al.* [95], optimal mode amplitude scaling and by comparing mode frequencies to flow spectral information from pressure probe and side-load signals. The sparsity-promoting algorithm solves a convex optimization problem to find an optimal subset of modes that best approximates the snapshot sequence.

Results: The DMD captured a helical mode linked to a peak in the side-load spectrum for the higher nozzle pressure ratio simulated. Not all peaks in the side-load spectrum could be linked to the DMD modes. For the lower nozzle pressure ratio, the most dominant mode had an azimuthal wavenumber $m = 2$. This mode could, if properly excited, cause ovalization of the nozzle itself, a phenomenon well known in nozzle research.

Comments: Several low frequency modes with high amplitudes were found to be significantly influenced by the resolved turbulence. This results in their structure being ”noisy” and their behavior hard to interpret. This is similar to the experience with performing DMD on the LES data in Paper C.

Division of Work: Ragnar Lárusson generated the computational mesh, set up and ran all simulations, post processed results along with writing most of the paper. The Second author, Markus Olander Burak, wrote the parallel DMD code and the script for the sparsity-promoting computations. He also wrote Sections IV.A and B on mode scaling and the sparsity-promoting algorithm, respectively. Together the co-authors supervised and provided support regarding solvers and many other technical issues. They provided invaluable help with the analysis of the results and writing of the paper.

7 Unpublished Results

7.1 Transient Nozzle Start-up Simulations

A transient nozzle start-up was simulated using the same nozzle contour and Detached Eddy Simulation (DES) set-up as in Lárusson et al. [6]. The nozzle pressure ratio (NPR) was linearly increased from 1 to 40 over a normalized time period of $tv_e/D_t = 1,192$. Time has been nondimensionalized using the throat diameter, D_t, and the exit velocity, v_e, obtained from quasi one dimensional isentropic calculations.
Given the relatively high computational cost of the simulation, an affordable NPR increase rate was chosen that is significantly higher than a realistic rocket engine start-up rate by at least an order of magnitude.

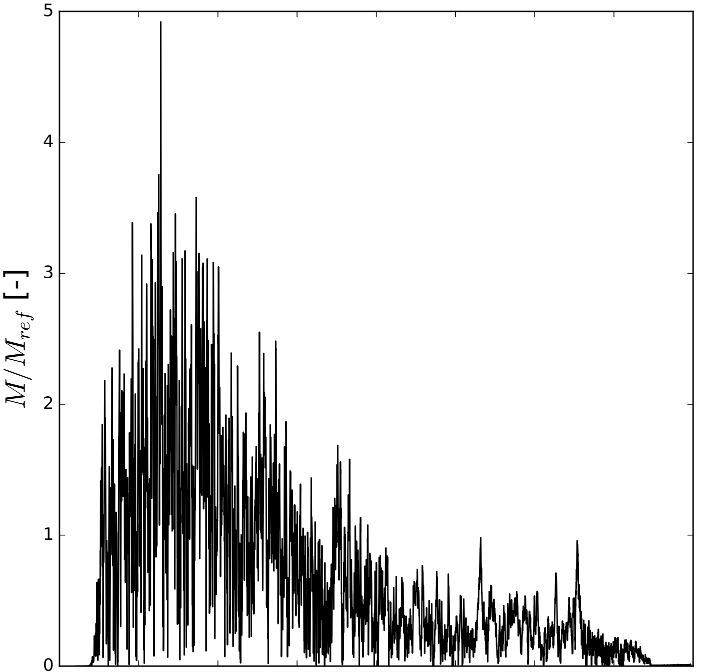

Figure 7.1: *DES prediction of side-loads acting on the VOLVO S6 nozzle during a linear increase of inlet pressure.*

Figure 7.1 shows the DES prediction of the nozzle side-loads during the NPR ramp. The side-load is presented in terms of a normalized moment around the nozzle throat,

M/M_{ref}, where M_{ref} is the highest aerodynamic side-load measured for the same nozzle contour in a previously conducted test campaign by Östlund et al. [113]. The figure shows a steep rise of the side-loads from $NPR \approx 2.5$ to $NPR \approx 7$, beyond which side-loads steadily decline. This trend is different from what is seen in side-load measurements by Östlund et al. [113] reprinted here in Figure 7.2. There we see a steady increase in the side-loads with maximum levels much closer to full flowing conditions. In Figure 7.2, the operating condition of the nozzle is expressed as off design parameter n:

$$n = \frac{p_{e,ff}}{p_a}, \tag{7.1}$$

where $p_{e,ff}$ is the theoretical nozzle exit wall pressure for a full flowing nozzle at the current NPR and p_a is the ambient pressure. This means that an increase in n corresponds to an increase in NPR and, at $n = 1$, the nozzle flow is ideally expanded.

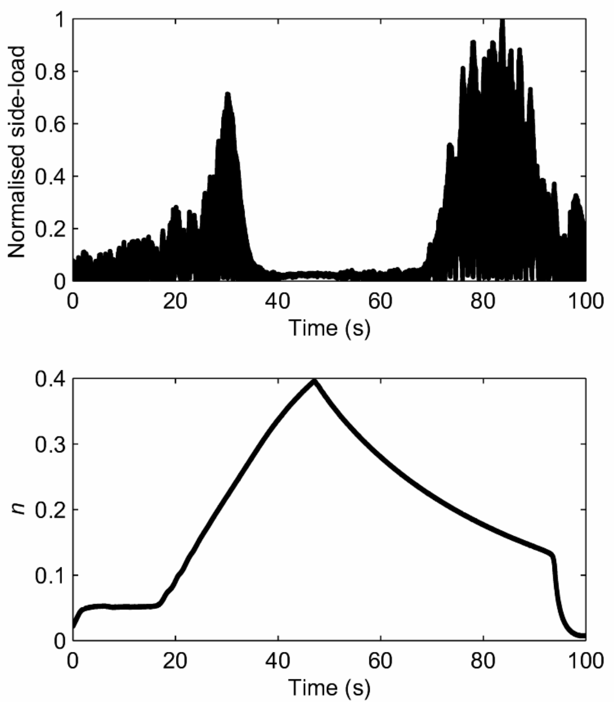

Figure 7.2: *Experimentally measured side-loads acting on the VOLVO S6 nozzle, reprinted from Östlund et al. [113] with permission.*

The NPR increase in Figure 7.2 is not linear during the whole start-up (and shut-down), and the time duration is two orders of magnitude greater than the linear ramp in the DES. We therefore switch the focus to side-load measurements from a cold flow test on another TIC nozzle performed at DLR's[14] nozzle test facilities in Lampoldshausen, Germany.

---

[14] DLR is the German Aerospace Centre

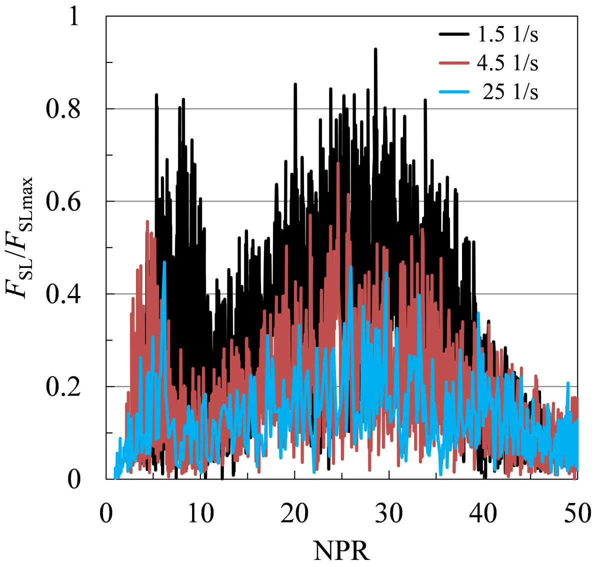

Figure 7.3: *Experimentally measured side-loads acting on a TIC nozzle for three different NPR gradients. Reprinted from Stark and Génin [42] with permission.*

Figure 7.3 shows the DLR side-load measurements that were originally published by Stark and Génin [42]. The figure shows side-load measurements for three different rates of NPR increase: 1.5 NPR/s, 4.5 NPR/s and 25 NPR/s. These rates were fairly constant during the test, and their fastest NPR rate differs from the DES ramp by one order of magnitude. The figure shows that an increase in NPR rate reduces the side-load amplitude while the curve's shape remains similar. Two side-load peaks are visible in the figure, one for $NPR < 10$ and another for $NPR \approx 25$ to $NPR \approx 30$. Stark and Génin [42] provide the following explanations for these peaks:

- It is believed that the boundary layer is laminar in the throat area as a consequence of high flow acceleration and a short distance downstream of the throat the boundary layer undergoes a laminar to turbulence transition. Turbulent boundary layers are known to withstand higher adverse pressure gradients compared to laminar boundary layers and therefore, at low NPR's, when the separation occurs in the transition area the separation point can quickly shift downstream as the boundary layer transitions. A slight asymmetry in the transition line along the circumference causes increased asymmetry in the separation line due to this shift, resulting in a side-load magnification. Furthermore, the Mach disc may tilt in the process so that part of the flow reattaches to the nozzle wall causing what Stark and Génin call a partial restricted shock separation (pRSS) which can enhance the side-load even further.

- Stark and Génin believe that the side-load rise at higher NPRs is caused by the movement of the contact point between the reflected shock and the shear layer across the nozzle exit plane. The definition and location of the contact point is shown in the schematic drawing of the shock system in Figure 7.4, as described by Stark and Génin [42]. The side-load rise here is linked to the sudden decrease in the area which the ambient air can enter through into the separation zone. This sudden change happens as the shape of the shear layer which is moving through the nozzle exit, goes from a cylindrical shape with a relatively constant diameter to a conical shape, see Figure 7.4. This mechanism was also described by Stark and Wagner [40] in a similar study.

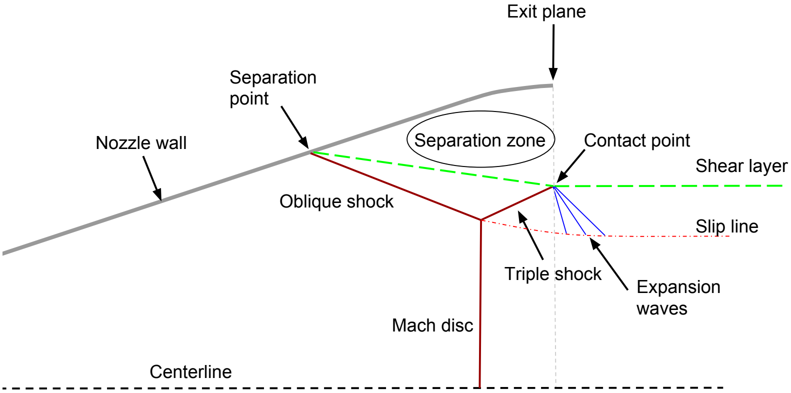

Figure 7.4: *Schematic drawing and nomenclature of free shock separation as described by Stark and Génin [42] and Stark and Wagner [40].*

There is no significant side-load rise at NPRs above 10 in the DES results. It therefore seems that there is no enhancement of side-loads in the DES when the contact point exits the nozzle. The side-loads reach their maximum levels at $NPR \approx 7$ in the DES, similar to what the DLR measurements show. However, this peak in the DES data cannot be attributed to boundary layer transition because, by using the log-law wall function, a turbulent boundary layer is assumed everywhere on the nozzle walls.

Figure 7.5 a) shows the pressure field during the DES simulation at $NPR \approx 7$ when the side-load amplitude reaches its maximum. The separation seems fairly symmetrical, and an animation of the simulation shows no partial reattachment (pRSS). The separation shock remains virtually symmetric throughout the simulation and it is therefore likely that the main reason for the side-loads is pressure fluctuations within the separated

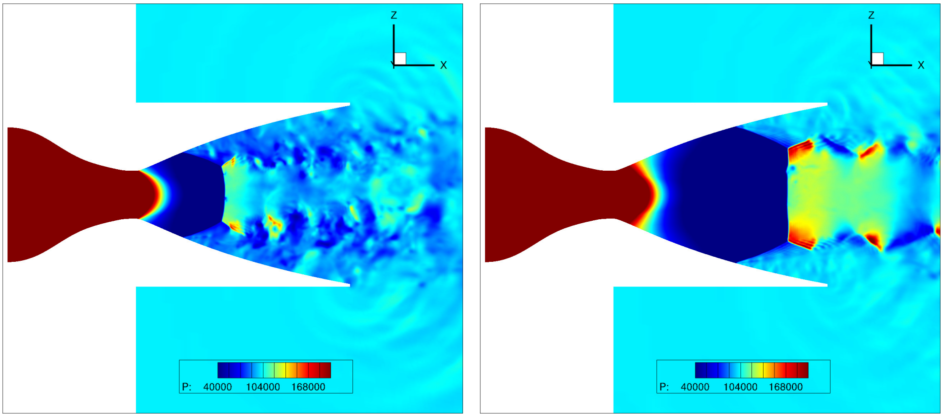

(a) $NPR \approx 7$

(b) $NPR \approx 17$

Figure 7.5: *Nozzle pressure field at two instances during the transient start-up simulation shown in Figure 7.1. Values are in Pascals.*

region. That explains why the maximum side-load is reached at $NPR \approx 7$, as turbulent instability seems to reach its maximum around that point. Figure 7.6 a) shows the level of fine scale turbulence within the nozzle at $NPR \approx 7$. Here the jet inside the nozzle becomes very unstable and asymmetric, and the animations hint at a helical mode being active in the nozzle although, this needs further analysis to confirm. The separation line itself remains symmetric, however. The pressure fluctuations are therefore not only generated by stochastic turbulence but also by lower frequency fluctuations caused by the movement of the jet. As the NPR rises, the jet stabilizes somewhat and the separation zone shrinks, causing a decline in side-loads. Figure 7.6 b) shows that there are fewer fine scale turbulent structures inside the separated region at $NPR \approx 22$.

There are sudden rises in the side-load in Figure 7.1 at $NPR \approx 17$, 22 and 33. The first rise at $NPR \approx 17$ occurs just before the contact point leaves the nozzle, and, shortly after it leaves, the side-loads continue to decrease. The animations shown no clear clue as to why we see a side-load peak at $NPR \approx 22$ but it occurs shortly after the Mach disc has gone through the nozzle exit plane. The peak at $NPR \approx 33$, however, is caused by the disappearance of a small secondary recirculation bubble located just upstream of the nozzle lip. When the secondary recirculation bubble can no longer be sustained, the immediate downstream conditions of separation shock change quickly and the shock shifts to the nozzle lip. This bubble can be seen by streamline visualization of the velocity field shown in Figure 7.7, from a DES at a constant $NPR = 19.74$ (Lárusson et al. [6]).

Note the convex shape of the Mach disc at $NPR \approx 7$ in Figure 7.5 a) and the concave shape at $NPR \approx 28$ in Figure 7.5 b). This difference in Mach disc shape at high and low NPRs was also noticed in Schlieren photographs from a cold flow test of a TIC nozzle at DLR published by Stark and Wagner [40]. In the DES, the Mach disc showed a high degree of instability at high NPRs as small scale vortices were continuously formed just downstream of the Mach disc. These fine scale turbulent structures are clearly visible

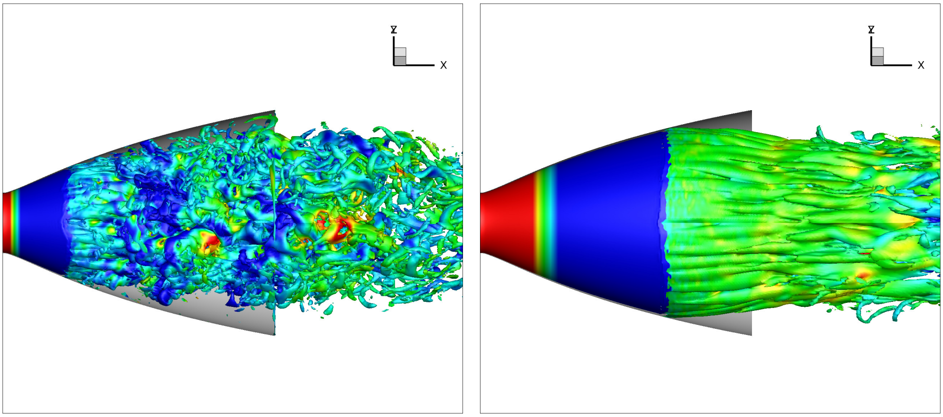

(a) $NPR \approx 7$ (b) $NPR \approx 22$

Figure 7.6: *Iso-surface of vorticity magnitude at two instances during the transient start-up simulation shown in Figure 7.1.*

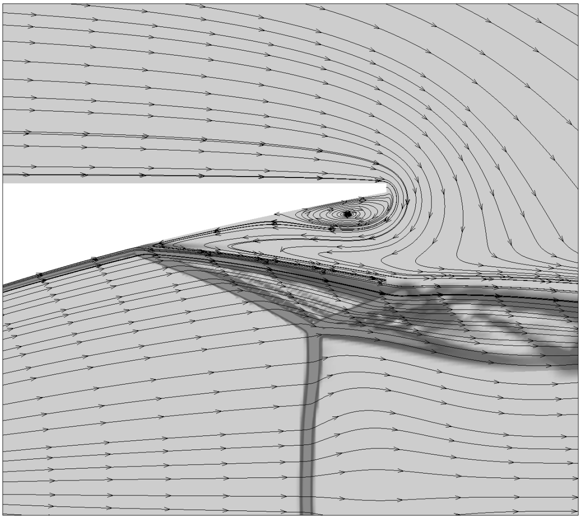

Figure 7.7: *DES at constant* $NPR = 19.74$*: Average streamlines visualizing the separated region on an* xz *plane going through* $y = 0$*. Shock waves are visualized with density gradient magnitude. From Lárusson et al. [6].*

in Figure 7.8, taken from Lárusson et al. [6] (Paper F), where DES was performed at constant NPR.

Based on the results above, it seems that the current DES methodology fails to recreate realistic side-load levels during a transient start-up sequence. This is because the separation line does not respond to the downstream unsteadiness and therefore remains nearly

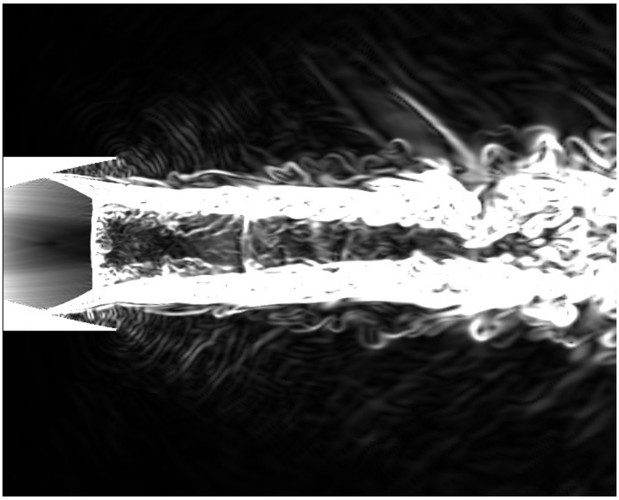

Figure 7.8: *DES at constant* $NPR = 19.74$*: Instantaneous density gradient magnitude. From Lárusson et al. [6].*

axisymmetric. Despite this, the simulation seems to capture some of the jet dynamics that could cause the separation line to move, were it able to. We see, for example, high fluctuations of the jet itself at low NPRs and a sudden increase of side-load levels just before the contact-point exits the nozzle. It would not be surprising that these events would be amplified if the separation shock reacted as it should. A possible remedy could include a better wall function or using a low-Reynolds number turbulence model to better capture the dynamics of the boundary layer. The second option, however, significantly increases the computational cost of the simulation, especially for an explicit solver where time step size restrictions become severe. An implicit time marching scheme would be needed to soften these restrictions. There is a possibility that a laminar-turbulent transition model is needed as well in order to accurately predict the initial side-load increase seen in the DLR measurements. Furthermore, the high NPR ramp rate in the DES could perhaps suppress the side-load increase caused by the contact point exiting the nozzle, as seen in the DLR measurements.

7.2 DMD Analysis of a TIC Nozzle. A Cooperation with DLR Lampoldshausen

The German Aerospace Center (DLR) in Lampoldshausen has a long history of experiments on supersonic nozzle flows. From conventional to new advanced contour designs [51], the test campaigns over the last ten years have focused on flow separation [40], side-load generation [42], contour ovalization [114], and dual bell nozzle transitional behavior [115]. A recent test campaign published by Génin and Startk [51] focused on spectral analysis of measurements from test of various nozzles with a truncated ideal contour (TIC). These nozzles varied in dimensions depending on their Mach number design, truncation location and wall angle. In short, the results showed a frequency peak in the measurements at 815Hz that was virtually independent of the feeding pressure. Furthermore, a higher frequency peak was identified with frequency around 1500Hz that varied with the feeding pressure. The peak first appears when the Mach disc is outside of the nozzle and from that point on its frequency decreases with increasing feeding pressure. Additional peak at 1105 Hz was found in the pressure measurements from a pressure sensor placed at the nozzle lip facing downstream. This peak only appeared in the signal of this sensor.
A DMD analysis of an axisymmetric URANS simulations of the same TIC was performed by the author of this thesis following his study visit to DLR Lampoldshausen. The aim was to see if any of the DMD modes would match one of the dominating frequencies observed in the experimental data. Three different NPRs were tested and are listed in Table 7.1. The 2D-URANS methodology applied here is the same as in the appended Papers B, C and E. That is, the URANS simulation is excited by a step increase in inlet pressure, using a converged RANS flow field of a lower NPR as an initial solution. The URANS simulation's response is then sampled and the samples used in the DMD algorithm to extract the modes. Since the URANS simulation is axisymmetric, only axisymmetric modes can be detected by the DMD analysis.

Table 7.1: Nozzle pressure ratios (NPRs) of the 2D-URANS DMD analysis.

NPR:	40.8	44.6	48.0

7.2.1 Computational Set Up

The computational set-up was similar to that of Papers B, C, and E. That is, a realizable k–ε turbulence model with log-law wall functions was applied. At DLR Lampoldshausen the cold flow tests at test bench P.2 are performed by feeding highly pressurized dry nitrogen to the nozzle. Gas properties of Nitrogen were therefore used in the simulations. Air is around 78% Nitrogen by volume so the difference in gas properties between air and Nitrogen are small. Therefore it was deemed safe to assume the same gas properties in the nozzle flow and in the ambient. Absorbing boundary conditions were applied on all boundaries except at the outlet where static pressure was applied. Using non-reflective boundary at the nozzle inlet resulted in strong fluctuating mode within the convergent part that dominated all other modes and contaminated the results in a way that other modes showed strong influence of the internal mode. Interestingly, this did not happen in the 2D-URANS DMD analysis of the VOLVO S6 nozzle.

The computational grid, shown in Figure 7.9, comprised roughly 70,000 cells.

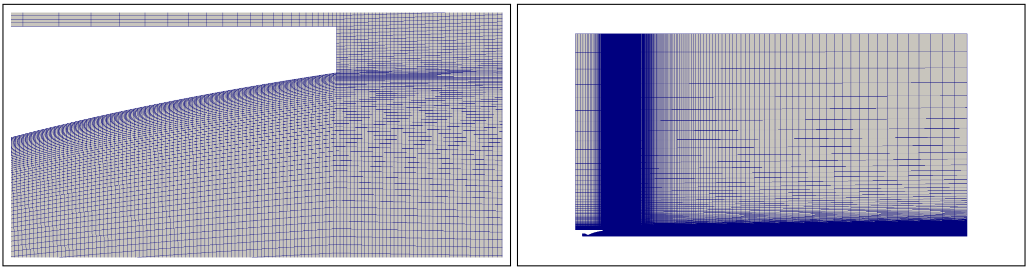

Figure 7.9: *Computational grid.*

7.2.2 Results

The steady state RANS simulations predicted the separation location fairly well as can be see in Figure 7.10. The wall pressure down stream of the separation, however, is over predicted.

Figure 7.11 shows the Mach number of the steady state RANS solutions. The figure shows that in all cases the Mach disc lies downstream of the nozzle exit. It also shows the relatively small difference in separation location between the cases. Note the increase in strength of the shocks downstream of the Mach disc with increasing NPR.

The norm $||\mu^{20}\phi||$, where μ is the eigenvalue and ϕ is the DMD mode, is shown in Figure 7.12. The spectra for $NPR = 40.8$ in Figure 7.12 a) shows the strongest[15] modes distributed relatively evenly across the frequency range. For the two higher NPRs, in Figures Figure 7.12 b) and c) the strongest modes found are at $f \approx 400$ and both cases show a clear decline in strength for $f > 1000$Hz.

Figure 7.13 shows the strongest mode for $NPR = 40.8$ at $f = 1500$Hz. Strong fluctuations are visible in the jet's core, especially in the Mach disc and the subsonic area downstream of it. The second shock downstream of the Mach disc shows high fluctuations as well. Notice the change in the fluctuation sign within the Mach disc. Animation of the mode shows that the Mach disc fluctuations are not purely axial but experience a 180° phase shift in the radial direction that moves radially through the Mach disc and continues through the triple shock[16]. There is a visible acoustical wave that originates from where the triple shock meets the edge of the shear-layer, also known as the contact point, marked with x in the figure. This wave has stronger radiation in the downstream direction but there is a weaker acoustical wave that travels upstream from the contact point as well, providing feedback to the separation point

Figure 7.14 shows the strongest mode within the frequency range 0Hz to 1000Hz for

---

[15] Here we refer to modes of high and low norm as strong and weak, respectively.

[16] See Figure 2.3 in Section 2.2 for the definition of the Mach disc and the triple shock

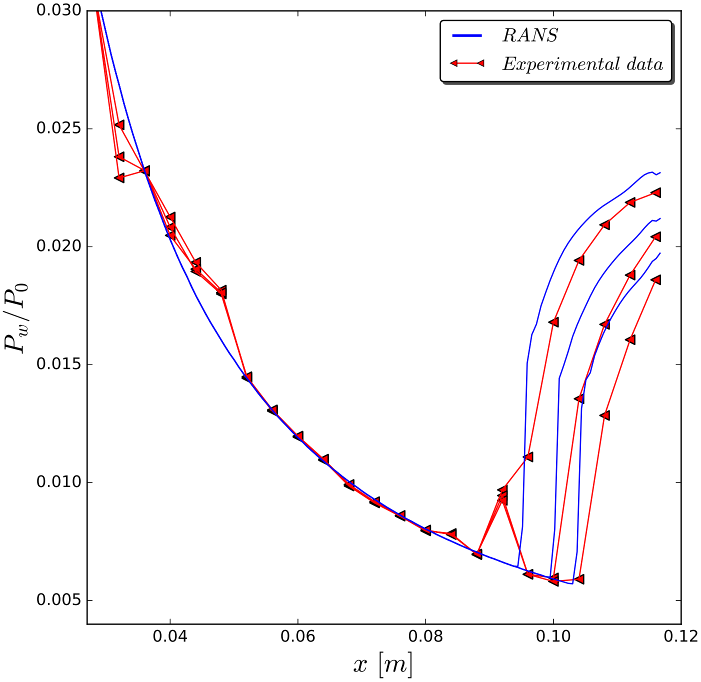

Figure 7.10: *Nozzle wall pressure for all three simulated NPRs. To distinguish between NPRs in the figure, remember that separation location moves downstream with increased NPR.*

$NPR = 40.8$. Animation of this mode showed a pure axial fluctuation of the shocks with a weak upstream traveling acoustical wave outside of the jet. The acoustical wave originates much further downstream than the figure extends. The strongest modes of $NPR = 44.6$ and 48.0 are shown in Figure 7.15 and 7.16, respectively. They have only a slightly higher frequency than the mode in Figure 7.14 and animations show that their transient behavior is similar.

7.2.3 Discussion

The strongest mode for $NPR = 48$ is within the frequency range of the higher dominating frequency found in experimental measurements. However, the strongest modes of the other two NPRs have much lower frequencies. It is therefore not possible to say with any confident that the mode in Figure 7.13 is the same mode observed in the experiments.
If we assume that it is not, then likely explanations for why that mode is not within the DMD results are that the modes associated with the frequencies observed in the experiments are not axisymmetric, hence not possible to obtain with axisymmetric

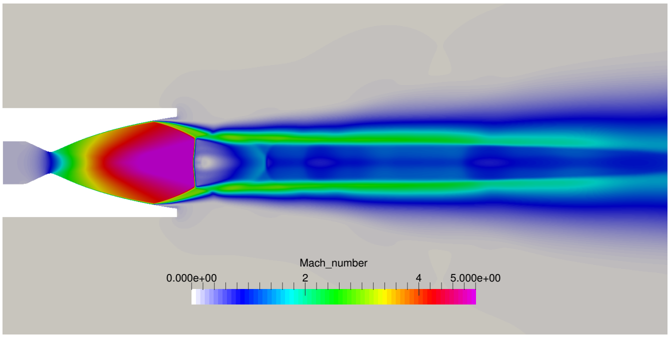

(a) *NPR=40.8*

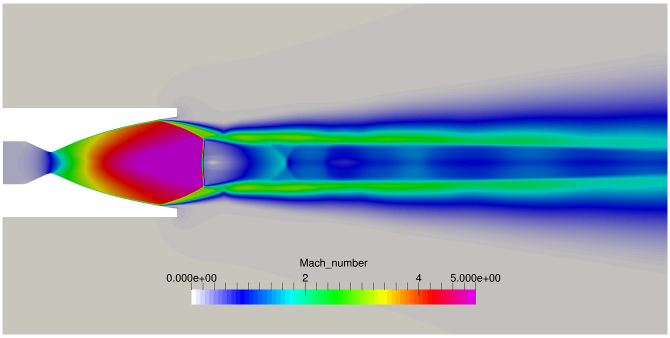

(b) *NPR=44.6*

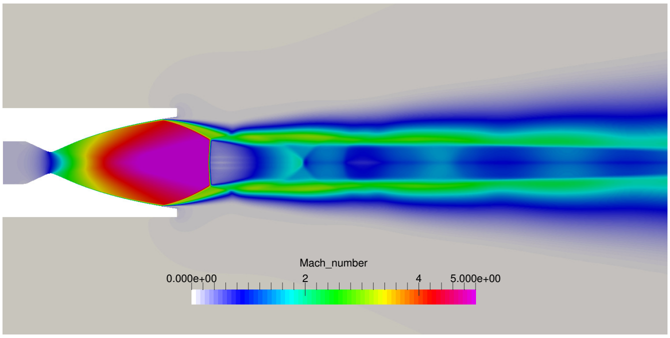

(c) *NPR=48.0*

Figure 7.11: *Mach number of the steady state RANS solution.*

simulation, or that they were not triggered in the excitation of the URANS flow field. It is also possible that the modes are test bench dependent, that means that they could not be found in a simulation with only the nozzle geometry. However, it is unlikely that the higher dominant frequencies in the experiments are test bench dependent as they showed a clear dependence with the NPR.
Note as well that the 815Hz dominant frequency observed in experiments was not among

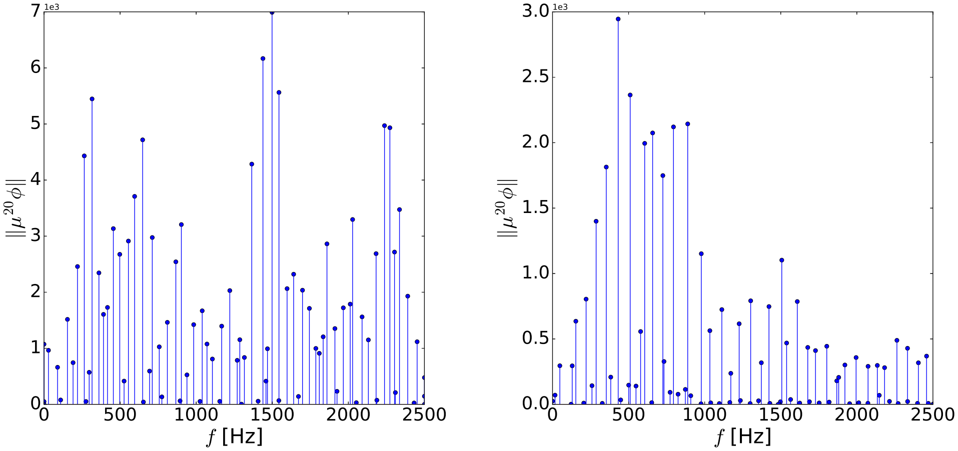

(a) *NPR=40.8* (b) *NPR=44.6*

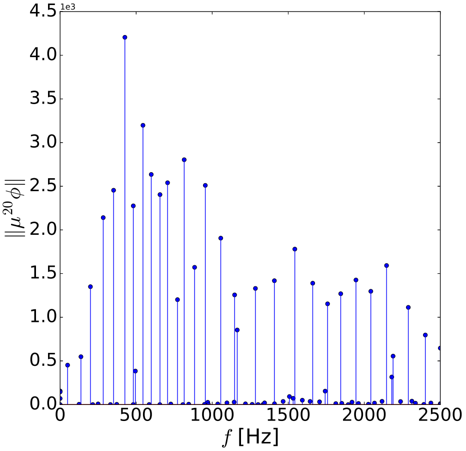

(c) *NPR=48.0*

Figure 7.12: *Norms, $||\mu^{20}\phi||$, and frequencies, f, of the DMD modes.*

the strongest DMD modes in this study. Neither was any mode with a strong upstream radiation of around 1100Hz as was found in experiments.

Despite the failure to predict the experimentally observed frequencies, the results are still interesting for a few reasons. One is the fact that no strong modes were found above 1000Hz for the two higher NPRs while the strongest mode for the lowest NPR was at 1500Hz. Interestingly, the acoustical wave found outside the jet in that mode seems to originate from the contact point. As discussed in the previous chapter, the contact point

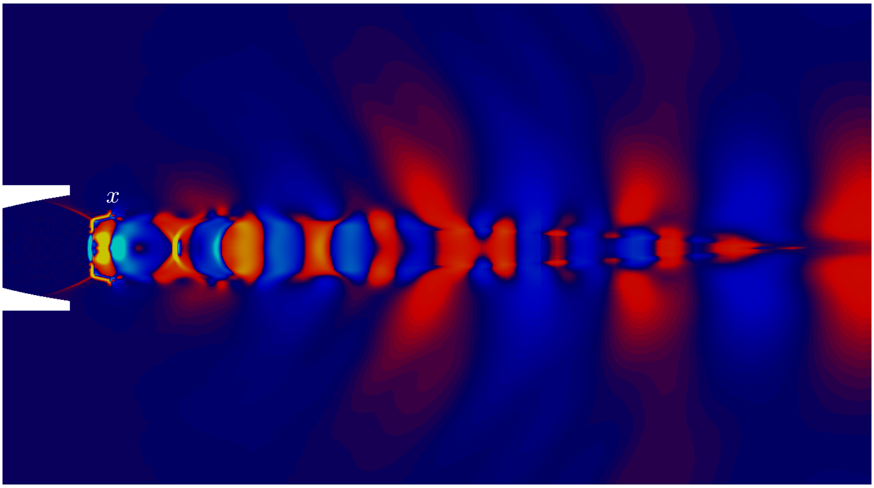

Figure 7.13: *NPR=40.8. DMD mode* $f = 1500Hz$. *Pressure perturbation field,* p'.

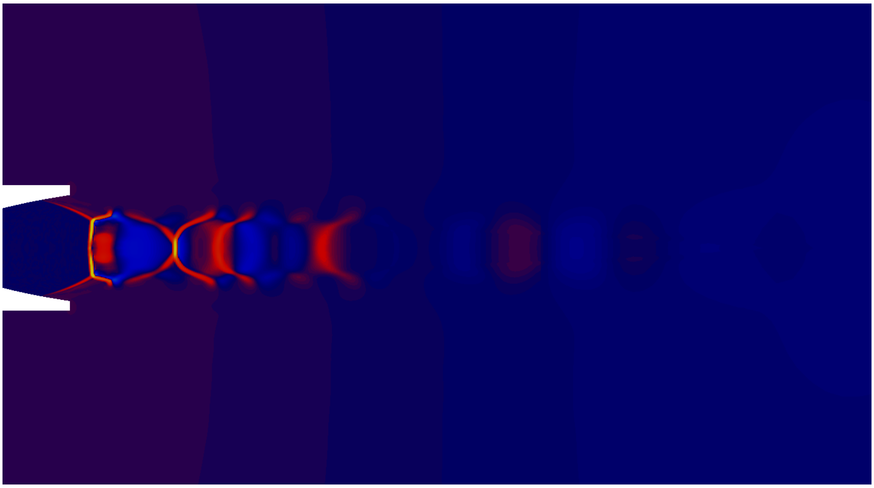

Figure 7.14: *NPR=40.8. DMD mode* $f = 315Hz$. *Pressure perturbation field,* p'.

is believed to play an important role in side-load generation in a start-up transient of a TIC nozzle. Furthermore, a similar mode was found in the Arnoldi analysis for the VOLVO S6 nozzle in Paper A. That mode showed a similar acoustical wave and a phase shift in the Mach disc.

The Arnoldi analysis in Paper A also showed that the least damped modes lie in a similar frequency range as the strongest modes of the two higher NPRs in this DMD analysis. Moreover, their shape and transient behavior were similar.

An attempt was made to perform an Arnoldi anlysis on the DLR TIC nozzle but instability issues with the flow solver were not resolved. The instabilities stemmed from where the

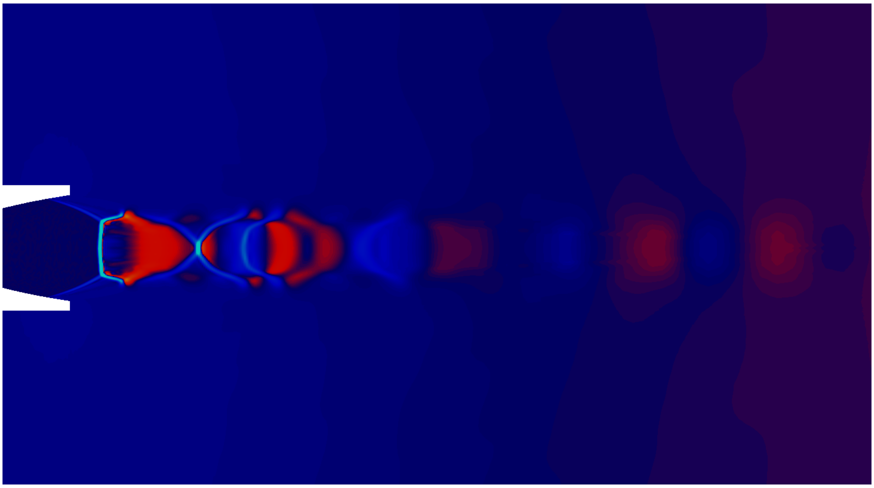

Figure 7.15: *NPR=44.6. DMD mode* $f = 431Hz$*. Pressure perturbation field,* p'*.*

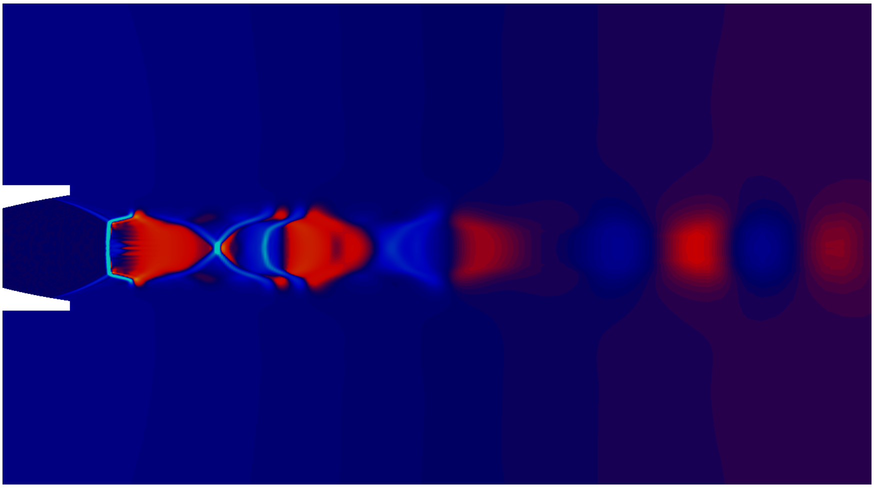

Figure 7.16: *NPR=48.0. DMD mode* $f = 431Hz$*. Pressure perturbation field,* p'*.*

Mach disc and the symmetry axis meet.

8 Conclusions and Future Directions

It has now been shown that the Arnoldi and the DMD methodologies are capable of extracting dynamically important modes in supersonic nozzle flow with separation and strong shocks. The advantage of the Arnoldi method is its capability to extract modes with higher azimuthal wave numbers on two dimensional grids. This advantage was demonstrated by the method's impressively accurate prediction of a helical screech mode of a conical nozzle under slightly overexpanded conditions. This mode compared remarkably well with LES results, both in frequency and acoustic radiation. However, the $k-\varepsilon$ model equations are ill-suited for linearization and therefore could not be included in the linear Navier-Stokes solver. As a compromise a frozen turbulent viscosity field was added to the laminar viscosity in the linear solver in Paper A. This resulted in uncontrolled instability originating just upstream of the separation point, causing the solution to diverge. As a working solution, the linear Navier-stokes solver was run with only laminar viscosity and in fact that proved to be more stable than using a linear Euler[17] equation solver. Issues with stability of the linear solver were present elsewhere. For example, a low-Reynolds number turbulence model resulted in instabilities near the wall, likely caused by high flow gradients and/or by high aspect ratio grid cells. Therefore, a wall function was needed to relax the grid density requirements near the wall. Furthermore, an Arnoldi analysis for a flow in a TIC nozzle geometry provided by DLR failed due to stability issues originating from the Mach disc near the symmetry axis. This issue could unfortunately not be resolved.

When comparing the two modal decomposition methods the 2D-URANS DMD analysis produced in some cases modes nearly identical to some of the Arnoldi modes. These modes were typically the least damped modes. It seems that more damped modes were either not excited by the URANS perturbation or that the DMD was not able to extract them from the snapshots. An inability of the DMD to extract some of the more damped modes could be caused by contamination in the snapshots from spurious modes due to aliasing effects or high frequency numerical oscillations. However, as reported in Paper E, modes associated with transonic resonance in a conical nozzle were found in a 2D-URANS DMD analysis. The modes showed a standing wave between the separation shock and the nozzle exit, as experimental observations from Zaman *et al.* [24] had indicated. This showed that the mechanism of transonic resonance in nozzles can be triggered in a URANS simulation and that the mode in this case is axisymmetric.

The DMD was also applied to a Detached Eddy Simulation (DES) of a separated nozzle flow. Because the DES is three dimensional, the DMD was capable of extracting helical modes that can potentially give rise to side-loads. In one case a helical mode could be linked to a peak in the DES side-load spectrum. An ovalization mode with azimuthal wave number $m = 2$ was also detected in the DES-DMD analysis. Interestingly, this mode was only present for the lower NPR of the two simulated.

In all of the DMD analyses, identifying converged and important modes was a challenge. The changing of the singular vector projection basis, also known as low-rank DMD, served well in the 2D-URANS anlysis in Papers B to E. However, a thorough study of the low-rank DMD using a data set with known underlying oscillating modes and an added random noise would be needed to give a better estimation of the accuracy of this method. In fact, in a recent DMD analysis by Burak *et al.* [116], compared the performance of the low-rank DMD method and the sparsity-promoting method [95] on shadowgraph imagery and the results indicated that the low-rank DMD failed to identify low energy modes such as harmonics of the dominant frequency mode. Meanwhile, the sparsity-promoting method successfully identified these modes. The combination of the sparsity-promoting method, optimal mode amplitude scaling and comparing mode frequencies to flow spectral information proved successful in the DMD analysis of the DES data. Using all of these methods turned out to be important since no individual method was capable of identifying all of the modes of interest.

---

[17] The Euler flow equations include no viscous terms

The sampling rate in the DES-DMD analysis was limited as a result of memory constraints. Sampling three dimensional snapshots, even if they only contain parts of the domain, requires a great deal of computer memory. The large difference in the time resolution of the DES and the time resolution of the snapshot data caused significant aliasing effects. The sparsity-promoting method identified important low frequency modes, but these modes were contaminated with noise. This shows that care is needed in determining the sampling rate. It could be beneficial to explore methods to circumvent this issue. One possibility is to interpolate the snapshot data onto a coarser grid, thereby decreasing the size of each snapshot to make possible a faster sampling rate. One could also consider filtering the snapshots. There exist several publications concerning how to reduce the effects of noise and sub Nyquist sampling rate in DMD analyses [98, 117]. For example, Tu *et al.* [118] presented a method of combining slowly sampled PIV[18] velocity fields with high time-resolution hot-wire velocity data to better capture dominant frequencies and their modes, including those with higher frequency than the Nyquist frequency of the PIV. This could perhaps be used in a highly resolved CFD simulation by combining probe data with three dimensional snapshots.

The DES of separated flow in the VOLVO S6 nozzle showed some promising results. However, the simulated nozzle side-load levels are likely lower than would be expected in experiments due to an insufficient response of the separation point to downstream instabilities. Some avenues of improvement were mentioned, such as exploring other wall functions or low-Re turbulence models and the use of implicit time marching. Wall Modeled LES (WMLES) [119], which resolves the upper layers of the boundary layer, should also be considered among future possibilities as computational resources become greater. It could be that resolving parts of the incoming boundary layer is more important to side-load generation than is generally believed. The need for better tuning of the DES constant C_{DES} was also mentioned in Section 3.5.

Finally, the importance of simulating a transient nozzle start-up, or shut-down, should be stressed, as some side-load generating flow dynamics are present only in such cases. The transient start-up simulations presented in Chapter 7.1 did not show expected side-load levels but did feature flow characteristics that are possibly linked to the side-load generation observed in experiments by Stark and Génin [42].

---

[18] Particle Image Velocimetry.

References

[1] R. Lárusson, N. Andersson, L.-E. Eriksson, and J. Östlund. Linear Stability Analysis Using the Arnoldi Eigenmode Extraction Technique Applied to Separated Nozzle Flow. *Proc. of the 49th AIAA/ASME/SAE/ASEE Joint Propulsion Conference* (2013). July 14-17, San Jose, CA, USA.

[2] R. Lárusson, N. Andersson, L.-E. Eriksson, and J. Östlund. Comparison of Eigenmode Extraction Techniques for Separated Nozzle Flows. *Proc. of the 50th AIAA/ASME/SAE/ASEE Joint Propulsion Conference* (2014). July 28-30, Cleveland, Ohio, USA.

[3] R. Lárusson, H. E. Hafsteinsson, N. Andersson, and L.-E. Eriksson. Investigation of Supersonic Jet Flow Using Modal Decomposition. *Proc. of the 20th AIAA/CEAS Aeroacoustics Conference* (2014). June 16-20, Atlanta, GA, USA.

[4] R. Lárusson, H. E. Hafsteinsson, N. Andersson, and L.-E. Eriksson. Investigation of Screech in Supersonic Jet Using Modal Decomposition. *Proc. of the 27th Nordic Seminar on Computational Mechanics* (2014). October 22-24, Stockholm, Sweden.

[5] R. Lárusson, N. Andersson, and J. Östlund. Dynamic Mode Decomposition of a Separated Nozzle Flow with Transonic Resonance. *AIAA Journal* (2017). Accepted for publication.

[6] R. Lárusson, N. Andersson, and J. Östlund. Hybrid RANS-LES Simulation of Separated Nozzle Flow. *Proc. of the 52nd AIAA/ASME/SAE/ASEE Joint Propulsion Conference* (2016). July 25-27, Salt Lake City, UT, USA.

[7] R. Lárusson, M. Olander Burak, N. Andersson, and J. Östlund. Dynamic Mode Decomposition Applied to a Detached-Eddy Simulation of Separated Nozzle Flow. *Proc. of AIAA SciTech Forum* (2017). January 9-13, Grapevine, TX, USA.

[8] *World Population Prospects 2015 – Data Booklet, (ST/ESA/ SER.A/377).* United Nations, Department of Economic and Social Affairs, Population Division. 2015. URL: `https://esa.un.org/unpd/wpp/Publications/Files/WPP2015_DataBooklet.pdf`.

[9] *The Space Report 2016.* Space Foundation. 2016. URL: `http://www.spacefoundation.org/sites/default/files/downloads/The_Space_Report_2014_Overview_TOC_Exhibits.pdf`.

[10] *World Bank national accounts data, and OECD National Accounts data files.* The World Bank. 2017. URL: `http://www.worldbank.org`.

[11] J. D. Anderson. *Modern Compressible Flow with Historical Perspective.* 3rd edition. McGraw-Hill, 2003.

[12] J. Östlund. *Flow processes in rocket engine nozzles with focus on flow separation and side loads.* ISSN 0348-467X. KTH Royal Institute of Technology in Stockholm, 2002.

[13] E. W. Larson, G. H. Ratekin, and G. M. O'Connor. Structural Response of the SSME Fuel Feedline to Unsteady Shock Oscillations Pt 2. *The Shock and Vibration Bulletin* (1982), pp. 177–182.

[14] T. Watanabe, N. Sakazume, and M. Tsuboi. LE-7A Engine Nozzle Problems During the Transient Operations. *38th AIAA/ASME/SAE/ASEE Joint Propulsion Conference* (2002).

[15] J. Shi. Rocket Engine Side Load Transient Analysis Methodology – A Practical Approach. *46th AIAA/ASME/ASCE/AHS/ASC Structures, Structural Dynamics and Materials Conference* (2005).

[16] G. Hagemann, J. Alting, and D. Preclik. Scalability for Rocket Nozzle Flows Based on Subscale and Full-Scale Testing. *Journal of Propulsion and Power* **19** (2003).

[17] N. Srivastava, P. T. Tkacik, and R. G. Keanini. Influence of nozzle random side loads on launch vehicle dynamics. *Journal of Applied Physics* **108** ().

[18] H. E. Hafsteinsson, L.-E. Eriksson, D. R. Cuppoletti, E. Gutmark, and E.Prisell. Active Suppression of Supersonic Jet Noise Using Pulsating Micro-Jets. *Proc. of the 50th AIAA Aerospace Sciences Meeting Including the New Horizons Forum and Aerospace Exposition* (2012).

[19] G. P. Sutton and O. Biblarz. *Rocket Propulsion Elements.* John Wiley & Sons, 2001.

[20] M. J. Zucrow. *Aircraft and Missile Propulsion.* John Wiley & Sons, 1958.

[21] S. J. Dick, ed. *Historical studies in the societal impact of spaceflight.* National Aeronautics and Space Administration, 2015. URL: `https://www.nasa.gov/connect/ebooks/index.html`.

[22] J. Östlund and B. Muhammad-Klingmann. Supersonic Flow Separation with Application to Rocket Engine Nozzles. *Mech. Rev.* **58** (2005), pp. 143–177.

[23] G. P. Sutton. *History of Liquid Propellant Rocket Engine.* American Institute of Aeronautics Astronautics, 2006.

[24] K. Zaman, M. Dahl, T. Bencic, and C. Loh. Investigation of a 'transonic resonance' with convergent-divergent nozzles. *Journal of Fluid Mechanics* **463** (2002), pp. 313–343.

[25] H. E. Hafsteinsson, L.-E. Eriksson, D. R. Cuppoletti, E. Gutmark, and E. Prisell. Active suppression of supersonic jet noise using pulsating micro-jets. *Proc. of the 50th AIAA Aerospace Sciences Meeting Including the New Horizons Forum and Aerospace Exposition* (2012).

[26] A. A. Aghababaie and R. Theunissen. Modeling Free Shock Separation Induced Side Loads in Overexpanded Rocket Nozzles. *AIAA Journal* **53** (2015).

[27] G. Guderley and E. Hantsch. Beste formen für achensymmetrische Überschallbdüsen. *Zeitschrift für Flugwissenschaften* **3** (1955).

[28] G. V. R. Rao. Exhaust Nozzle Contours for Optimum Thrust. *Journal of Jet Propulsion* **28** (1958).

[29] G. V. R. Rao. Approximation of optimum thrust nozzle contour. *ARS Journal* **30** (1960).

[30] G. Hagemann, H. Immich, T. G. Nguyen, and G. E. Dumnov. Advanced Rocket Nozzles. *Journal of Propulsion and Power* **14** (1998), pp. 620–634.

[31] L. H. Nave and G. A. Coffey. Sea Level Side Loads in High-Area-Ratio Rocket Engines. *Proc. of the 9th Propulsion Conference* (1973). AIAA paper 1973-1284.

[32] A. Hadjadj and M. Onofri. Nozzle flow separation. *Shock Waves* **19** (2009).

[33] F. Nasuti and M. Onofri. Shock structure in separated nozzle flows. *Shock Waves* **19** (2009).

[34] J. N. Murugan and R. N. Govardhan. Shock wave–boundary layer interaction in supersonic flow over a forward-facing step. *J. of Fluid Mech.* **807** (2016).

[35] N. A. Adams. Direct simulation of the turbulent boundary layer along a compression ramp at M= 3 and Reθ= 1685. *J. of Fluid Mech.* **420** (2000).

[36] G. Aubard, X. Gloerfelt, and J.-C. Robinet. Large-Eddy Simulation of Broadband Unsteadiness in a Shock/Boundary-Layer Interactioni. *AIAA Journal* **51** (2013).

[37] V. Ferriman and H. Sunley. Jet separation in conical nozzles. *Journal of the Royal Aeronautical Society* **68** (1964).

[38] A. Hadjadj and J.-P. Dussauge. Shock wave boundary layer interaction. *Shock Waves* **19** (2009).

[39] J. Mattsson, U. Högman, and L. Torngren. A sub-scale test programme on investigation of flow separation and side-loads in rocket nozzles. *Proc. of the 3rd European Symposium on Aerothermodynamics of Space Vehicles* (1998).

[40] R. Stark and B. Wagner. Experimental Study of Boundary Layer Separation in Truncated Ideal Contour Nozzle. *Shock Waves* **19** (2008).

[41] J. Ruf, D. McDaniels, and A. Brown. Details of Side Load Test Data and Analysis for a Truncated Ideal Contour Nozzle and a Parabolic Contour Nozzle. *Proc. of the 46th AIAA/SAE/ASEE Joint Propulsion Conference* (2010).

[42] R. Stark and C. Génin. Parametrical Study on Side Load Generation in Subscale Rocket Nozzles. *proc. of the 6th EUCASS Conference, Cracow, Poland* (2015).

[43] S. Deck and P. Guillen. Numerical Simulation of Side Loads in an Ideal Truncated Nozzle. *Journal of Propulsion and Power* **18** (2002), pp. 262–269.

[44] T. Shimizu, H. Miyajima, and M. Kodera. Numerical Study of Restricted Shock Separation in a Compressed Truncated Perfect Nozzle. *AIAA Journal* **44** (2006).

[45] T.-S. Wang. Transient Three-Dimensional Startup Side Load Analysis of a Regeneratively Cooled Nozzle. *Shock Waves* **19** (2002).

[46] S. Deck. Delayed Detached Eddy Simulation of the End-Effect Regime and Side-Loads in an Overexpanded Nozzle Flow. *Shock Waves* **19** (2009).

[47] B. J. Olson and S. K. Lele. A mechanism for unsteady separation in over-expanded nozzle flow. *Physics of Fluids* **25**.11 (2013), p. 110809. ISSN: 10706631. DOI: `10.1063/1.4819349`.

[48] R. Schwane, D. Perigo, and X. Yang. Unsteady Numerical Simulations of the Flow in a Truncated Ideal Contour Nozzle Under Free Shock Separation Conditions. *21st Applied Aerodynamics Conference. 23-26 June, Orlando, Florida* (2003). AIAA paper 2003-3676.

[49] R. Schwane and Y. J. Xia. Time-Accurate CFD Predictions and Data Validation for Side Load Generation by Flow-Structure Coupling in Over-Expanded Rocket Nozzles. *Math Model Algor* (2005).

[50] J. A. Moríñigo and J. J. Salvá. Numerical study of the start-up process in an optimized rocket nozzle. *Aerospace Science and Technology* **12** (2008).

[51] C. Génin and R. Stark. Experimental Investigation of cold flow TIC nozzles, a spectral analysis. *Proc. of the 52th AIAA/SAE/ASEE Joint Propulsion Conference* (2016). AIAA paper 2016-4668.

[52] C. A. Hunter. Experimental Investigation of Separated Nozzle Flows. *Journal of Propulsion and Power* **20** (2004).

[53] S. B. Verma and C. Manisankar. Origin of flow asymmetry in planar nozzles with separation. *Shock Waves* **24** (2014).

[54] D. Papamoschou, A. Zill, and A. Johnson. Supersonic flow separation in planar nozzles. *Shock Waves* **19** (2009).

[55] L. Davidson. *Fluid mechanics, turbulent flow and turbulence modeling.* Chalmers University of Technology. 2017. URL: `http://www.tfd.chalmers.se/~lada/postscript_files/solids-and-fluids_turbulent-flow_turbulence-modelling.pdf`.

[56] A. Favre. Turbulence: space-time statistical properties and behavior in supersonic flows. *Physics of Fluids* **23** (1983).

[57] B. E. Launder and D. B. Spalding. The Numerical Computation of Turbulent Flows. *Computer Methods in Applied Mechanics and Engineering* **3** (1973).

[58] L. Davidson. *An Introduction to Turbulence Models.* Chalmers University of Technology. 2016. URL: `http://www.tfd.chalmers.se/~lada/postscript_files/kompendium_turb.pdf`.

[59] J. Smagorinsky. General Circulation Experiments with the Primitive Equations. *Monthly Weather Review* **91** (1963).

[60] G. Erlebacher, M. Y. Hussaini, C. G. Speziale, and T. A. Zang. Toward the large-eddy simulation of compressible turbulent flows. *Journal of Fluid Mechanics* **238** (1992).

[61] A. Yoshizawa. Bridging between eddy-viscosity-type and second-order turbulence models through a two-scale turbulence theory. *Phys. Rev. E* **48** (1993).

[62] N. A. Adams and S. Hickel. Implicit Large-Eddy Simulation: Theory and Application. *Advances in Turbulence XII* **132** (2009).

[63] P. R. Spalart. Comments on the Feasibility of LES for Wing and on a Hybrid RANS/LES Approach. *Proc. of the 1st ASOSR Conference on DNS/LES* (1997).

[64] P. R. Spalart and S. R. Allmaras. A One-Equation Turbulence Model for Aerodynamic Flows. *Recherce Aerospatiale* **1** (1994).

[65] M. Strelets. Detached-Eddy Simulation of Massively Separated Flows. *Proc. of the 39th Aerospace Sciences Meeting and Exhibit* (2001).

[66] J. Yan, C. Mockett, and F. Thiele. Investigation of alternative length scale substitutions in Detached-Eddy simulation. *Flow, Turbulence and Combustion* **74** (2005).

[67] A. Shams, S. Girard, and P. Comte. Numerical Simulations of Shock-Induced Separated Flows in Overexpanded Rocket Nozzles. *Progress in Flight Physics* **3** (2012), pp. 169–190.

[68] P. R. Spalart, S. Deck, M. L. Shur, K. D. Squires, M. K. Strelets, and A. Travin. A new version of detached-eddy simulation, resistant to ambiguous grid densities. *Flow, Turbulence and Combustion* **74** (2005).

[69] F. R. Menter and M. Knutz. Adaptation of Eddy-Viscosity Turbulence Models to Unsteady Separated Flow Behind Vehicles. *Proc. of the Symposium on the aerodynamics of heavy vehicles: trucks, buses and trains.* (2002).

[70] J. Frohlich, C. P. Mellen, W. Rodi, L. Temmerman, and M. A. Leschziner. Highly resolved large-eddy simulation of separated flow in a channel with streamwise periodic constrictions. *J. Fluid Mech.* **526** (2005).

[71] J. Bredberg. On Two-equation Eddy-Viscosity Models. *Chalmers University of Technology, Internal Report 01/08* (2001). URL: `http://www.tfd.chalmers.se/~lada/postscript_files/jonas_report_lowre.pdf`.

[72] H. Wong. Theoretical Prediction of Resonance in Nozzle Flows. *Journal of Propulsion and Power* **21** (2005), pp. 300–313.

[73] A. A. Sergienko and A. V. Kirillov. Pulsating Loads on Propulsive Nozzles with Flow Separation. *Aviatsionnaya Tekhnika* (2000).

[74] W. E. Arnoldi. The principle of minimized iterations in the solution of the matrix eigenvalue problem. *Appl. Math.* **9** (1951), pp. 17–29.

[75] Y. Saad. Variations on Arnoldi's Method for Coupling Eigenelements of Large Unsymmetric Matrices. *Linear Algebra, and its applications* **34** (1980), pp. 269–298.

[76] L.-E. Eriksson and A. Rizzi. Computer-aided analysis of the convergence to steady state of discrete approximations to the Euler equations. *Journal of Computational Physics* **57** (1985), pp. 90–128.

[77] L.-E. Eriksson, L. Andersson, K. Lindblad, and N. Andersson. Development of a Cooled Radial Flameholder for the F404/RM12 afterburner: Part III Afterburner Rumble Prediction and Suppression. *Proc. of the 16th ISABE Conf, September 2003, Ohio, USA.* (2003). ISABE paper 2003-1060.

[78] L.-E. Eriksson and P. Moradnia. Computational Study of Mixed Hydrodynamic-Acoustic Waves in Gas Turbine Afterburner Flows. *proc. of the 14th AIAA/CEAS Aeroacoustics Conference, 5-7 May 2008, Vancouver, Canada.* (2008). AIAA paper 2008-2950.

[79] G. Jourdain and L.-E. Eriksson. Numerical Comparison Between the Dynamic Mode Decomposition and the Arnoldi Extraction Technique on an Afterburner Test Case. *proc of the 18th AIAA/CEAS Aeroacoustics Conference, 4-6 June 2012, Colorado, USA,* (2012).

[80] W. Edwards. Krylov Methods for the Incompressible Navier-Stokes Equations. *Journal of Computational Physics* **110**.1 (1994), pp. 82–102.

[81] H. Sheraton and P. Castle. Eigenvalues of the discretized Navier-Stokes equation with application to the detection of Hopf bifurcations. *Adv Comput Math* **1** (1993), pp. 337–356.

[82] R. Melnik and K. Zotsenko. Finite element analysis of coupled electronic states in quantum dot nanostructures. *Modelling and Simulation in Materials Science and Engineering* **12**.3 (2004), pp. 465–477.

[83] A. Dimitrov, H. Andrä, and E. Schnack. Singularities near three-dimensional corners in composite laminates. *Int. Journal of Fracture* **115**.4 (2002), pp. 361–375.

[84] T. Hayashi and S. Mukamel. Multidimensional Infrared Signatures of Intramolecular Hydrogen Bonding in Malonaldehyde. *Journal of Physical Chemistry A* **107**.43 (2003), pp. 9113–9131.

[85] P. J. Schmid and J. Sesterhenn. Dynamic mode decomposition of numerical and experimental data. *61st Annual Meeting of the APS Division of Fluid Dynamics, San Antonio, Texas* (2008).

[86] P. J. Schmid. Dynamic mode decomposition of numerical and experimental data. *Journal of Fluid Mechanics* **656** (2010), pp. 5–28.

[87] C. Rowley, I. Mezic, S. Bagheri, P. Schlatter, and D. Henningson. Spectral analysis of nonlinear flows. *Journal of Fluid Mechanics* **641** (2009), pp. 115–127.

[88] G. Jourdain, L.-E. Eriksson, S. Kim, and C. Sohn. Application of dynamic mode decomposition to acoustic-modes identification and damping in a 3-dimensional chamber with baffled injectors. *Journal of Sound and Vibration* **332**.18 (2013), pp. 4308–4323.

[89] S. Bagheri. Koopman-mode decomposition of the cylinder wake. *Journal of Fluid Mechanics* **726** (2013), pp. 596–623.

[90] M. Grilli, P. Schmid, S. Hickel, and N. Adams. Analysis of unsteady behaviour in shockwave turbulent boundary layer interaction. *Journal of Fluid Mechanics* **700** (2012), pp. 16–28.

[91] A. Seena and H. Sung. Dynamic mode decomposition of turbulent cavity flows for self-sustained oscillations. *Int. Journal of Heat and Fluid Flow* **32**.6 (2011), pp. 1098–1110.

[92] K. Chen, J. Tu, and C. Rowley. Variants of dynamic mode decomposition: Boundary condition, Koopman, and fourier analyses. *Journal of Nonlinear Science* **22**.6 (2012), pp. 887–915.

[93] I. Mezic. Analysis of fluid flows via spectral properties of the koopman operator. *Annual Review of Fluid Mechanics* **45** (2013), pp. 357–378.

[94] H. J. Tu. Dynamic Mode Decomposition: Theory and Application. *Ph.D. Thesis. Princeton University* (2013).

[95] M. R. Jovanović, P. J. Schmid, and J. W. Nichols. Sparsity-promoting dynamic mode decomposition. *Journal of Physics of Fluids* **26**.204103 (2014).

[96] A. Wynn, D. Pearson, B. Ganapathisubramani, and P. Goulart. Optimal mode decomposition for unsteady flows. *J. Fluid Mech.* **733** (2013).

[97] M. S. Hemati, M. O. Williams, and C. W. Rowley. Dynamic mode decomposition for large and streaming datasets. *Physics of Fluids* **26** (2014).

[98] M. S. Hemati, C. W. Rowley, E. A. Deem, and L. N. Cattafesta. De-Biasing the Dynamic Mode Decomposition for Applied Koopman Spectral Analysis of Noisy Datasets. *pre-print, arXiv:1502.03854* (2015).

[99] G. Jourdain and L.-E. Eriksson. Combustor Stability Analysis Based on Linearized Flow Solvers and Arnoldi-based Eigenmode Extraction Techniques. *proc. of the 16th AIAA/CEAS Aeroacoustics Conference, 7-9 June 2012, Stockholm, Sweden.* (2012).

[100] S. Balay, S. Abhyankar, M. F. Adams, J. Brown, P. Brune, K. Buschelman, L. Dalcin, V. Eijkhout, W. D. Gropp, D. Kaushik, M. G. Knepley, L. C. McInnes, K. Rupp, B. F. Smith, S. Zampini, and H. Zhang. PETSc Users Manual. *Tech. Rep. ANL-95/11 - Revision 3.6* (2015). Argonne National Laboratory.

[101] S. ABalay, W. D. Gropp, L. C. McInnes, and B. F. Smith. Efficient Management of Parallelism in Object Oriented Numerical Software Libraries. *in Arge, E., Bruaset, A. M., and Langtangen, H. P., eds., Modern Software Tools in Scientific Computing* (1997). Birkhäuser Press, pp. 163–202.

[102] N. Andersson. *G3D::Flow, A Code Framework for Simulation of Compressible and Incompressible Flows.* 2017. URL: `https://nikander.github.io/g3dflow/index.html`.

[103] L.-E. Eriksson. Linearized Navier-Stokes solver in "frequency/azimuthal mode number" domain based on axisymmetric steady-state reference flows. *Chalmers Research Report 2014:12* (2014). Chalmers Univeristy of Technology.

[104] L.-E. Eriksson. Development and Validation of Highly Modular Flow Solver Versions in G2DFLOW and G3DFLOW. *Internal report 9970-1162* (1995). Volvo Aero Corporation.

[105] SciPy.org. *A Python-based Ecosystem of Open-source Software for Mathematics, Science, and Engineering.* 2017. URL: `https://www.scipy.org/`.

[106] V. Hernandez, J. E. Roman, and V. Vidal. SLEPc: A Scalable and Flexible Toolkit for the Solution of Eigenvalue Problems. *ACM Transactions on Mathematical Software* **31** (2005).

[107] J. E. Roman, C. Campos, E. Romero, and A. Tomas. SLEPc Users Manual. *Tech. Rep. DSIC- II/24/02 - Revision 3.6, D. Sistemes Informàtics i Computació, Universitat Politècnica de València* (2015).

[108] O. Rask, S. Harrison, D. Munday, C. Harris, M. Mihaescu, and E. Gutmark. Jet Aircraft Propulsion Noise Reduction Research at University of Cincinnati. *Proc. of the 43rd AIAA/ASME/SAE/ASEE Joint Propulsion Conference* (2007). 8-11 July, Cincinnati, OH, USA.

[109] M. Olander Burak, L.-E. Eriksson, D. Munday, E. Gutmark, and E. Prisell. Experimental and Numerical Investigation of a Supersonic C-D Nozzle. *Proc of the 30th AIAA Aeroacoustic Conference* (2009).

[110] B. Gustafsson, L.-E. Eriksson, D. Cuppoletti, E. Gutmark, and E. Prisell. Nozzle Throat Optimization for Supersonic Jet Noise Reduction. *Proc. of the 50th AIAA Aerospace Sciences Meeting Including the New Horizons Forum and Aerospace Expositio* (2012). 9-12 January, Nashville, TN, USA.

[111] D. Munday, D. Cuppoletti, M. Perrino, E. Gutmark, M.Olander Burak, and L.-E. Eriksson. Supersonic Turbojet Noise Reduction. *Int. Journal of Aeroacoustics* **12** (2013), pp. 215–244.

[112] C. Loh and K. Zaman. Numerical investigation of transonic resonance with a convergent-divergent nozzle. *AIAA Journal* **40**.12 (2002), pp. 2393–2401.

[113] J. Östlund, T. Damgaard, and M. Frey. Side-Load Phenomena in Highly Overexpanded Rocket Nozzles. *Journal of Propulsion and Power* **20** (2004).

[114] C. Génin and R. Stark. Flow Separation Study in Stiff Ovalized Rocket Nozzles, Part I: Experimental Approach. *Proc. of the 51st AIAA/SAE/ASEE Joint Propulsion Conference* (2015). AIAA paper 2015-4153.

[115] C. Nürnberger-Génin and R. Stark. Experimental Study on Flow Transition in Dual Bell Nozzles. *Journal of Propulsion and Power* **26** (2010), pp. 497–502.

[116] M. O. Burak, K. M. B. Gustafsson, B. Malla, and E. Gutmark. Screech Noise Characterization using Dynamic Mode Decomposition and Shadowgraph Imagery. *Proc. of the 22nd AIAA/CEAS Aeroacoustic Conference* (2016).

[117] C. Pan, D. Xue, and J. Wang. On the accuracy of dynamic mode decomposition in estimating instability of wave packet. *Exp Fluids* **56** (2015).

[118] J. H. Tu, C. W. Rowley, J. N. Kutz, and J. K. Shang. Spectral analysis of fluid flow using sub-Nyquist-rate PIV data. *Exp Fluids* **55** (2014).

[119] U. Piomelli and E. Balaras. Wall-layer models for large-eddy simulations. *Annual Review of Fluid Mechanics* **34** (2002).